2015

Microindentation of Bi57In26Sn17 Lead-Free Alloy

Ruiting Zhao
University of Kentucky, rzh232@g.uky.edu

STUDENT AGREEMENT:

I represent that my thesis or dissertation and abstract are my original work. Proper attribution has been given to all outside sources. I understand that I am solely responsible for obtaining any needed copyright permissions. I have obtained needed written permission statement(s) from the owner(s) of each third-party copyrighted matter to be included in my work, allowing electronic distribution (if such use is not permitted by the fair use doctrine) which will be submitted to UKnowledge as Additional File.

I hereby grant to The University of Kentucky and its agents the irrevocable, non-exclusive, and royalty-free license to archive and make accessible my work in whole or in part in all forms of media, now or hereafter known. I agree that the document mentioned above may be made available immediately for worldwide access unless an embargo applies.

I retain all other ownership rights to the copyright of my work. I also retain the right to use in future works (such as articles or books) all or part of my work. I understand that I am free to register the copyright to my work.

REVIEW, APPROVAL AND ACCEPTANCE

The document mentioned above has been reviewed and accepted by the student's advisor, on behalf of the advisory committee, and by the Director of Graduate Studies (DGS), on behalf of the program; we verify that this is the final, approved version of the student's thesis including all changes required by the advisory committee. The undersigned agree to abide by the statements above.

Ruiting Zhao, Student

Dr. Fuqian Yang, Major Professor

Dr. Tom Dziubla, Director of Graduate Studies

MICROINDENTATION OF BI57IN26SN17 LEAD-FREE ALLOY

THESIS

A thesis submitted in partial fulfillment of the requirements for the degree of Master of Science in Material Science and Engineering in the College of Engineering at the University of Kentucky

By

Ruiting Zhao

Lexington, Kentucky

Director: Dr. Fuqian Yang, Professor of Material Science and Engineering

Lexington, Kentucky

2015

THESIS ABSTRACT

MICROINDENTATION OF BI57IN26SN17 LEAD-FREE ALLOY

There is great need to understand the mechanical properties of lead-free alloys—an alternative of lead-based alloys—to address the environmental problems associated with the use of lead-based materials in microelectronics. In this work, the microstructures of Bi57In26Sn17 lead-free alloy were examined using Optical Microscopy and Energy Dispersive X-ray Spectroscopy analysis. The micro-indentation technique was used to study the mechanical properties of Bi57In26Sn17 lead-free alloy. The experimental results of the hardness and contact modulus were presented and discussed. Local creep during the indentation was observed from the load-displacement curves. The Vickers hardness (HV) increases with the decrease of the indentation depth, suggesting that the alloy exhibits indentation size effect.

KEYWORDS: Micro-indentation, Bi-In-Sn alloy, lead-free alloy, Vickers hardness, reduced contact modulus, indentation size effect.

Ruiting Zhao

December 10th, 2015

MICROINDENTATION OF BI57IN26SN17 LEAD-FREE ALLOY

By

Ruiting Zhao

Fuqian Yang, Ph.D.

Director of Thesis

Tom Dziubla, Ph.D.

Director of Graduate Studies

December 10th, 2015

Date

ACKNOWLEDGEMENTS

I would like to thank my adviser, Dr. Fuqian Yang, for his substantial guidance and advice.

I would also like to thank Dr. Tongguang (Tony) Zhai and Dr. Yang-Tse Cheng for serving as my thesis committee members and for providing valuable comments and suggestions.

Thanks to my group members (Guangfeng Zhao, Wei Sun, Dr. Yuan Sun and Dr. Liping Bian) for their technical support, as well as all my classmates (Tiantian Zeng, Xiaowen Zhan, Faez Qahtani and Ben Reyes) and my friends in Auburn (Yating Chai, Shin Horikawa and Sadhwi Ravichandran) for the lab friendships and encouragement.

At last, I would like to express my appreciation to my family for their confidence in me from beginning to end.

Table of Contents

List of Tables

List of Figures

Chapter 1 :Introduction

1.1 Introduction

Environmental problems and human health problems due to the use of lead-based solders in microelectronics are being taken more seriously. These regulatory requirements aimed at lead-related production have resulted in a swift growth of the lead market price since 2006 [1]. This has led to great progress in the development of lead-free solder alloys. There is a great need to replace the lead-based solder alloys with the lead-free solder alloys. A tremendous demand on the relative information and properties about lead-free solder alloys had been shown in recent years.

Bi-In-Sn alloys among other lead-free alloys such as Sn-Bi, Sn-Ag-Cu [2], and Sn-Bi-In-Ag have been proposed to have great potential to become alternative solutions for lead-based alloy. With the addition of a moderate amount of Indium element, the ductility of Sn-Bi compound is greatly improved and the peak temperature decreased according to previous works. In previous works, tensile tests on the Sn-Bi-In lead-free alloys were performed, oxidation resistance was investigated, and even the creep behaviors of Sn-Bi-In lead-free alloy were studied [3] [4]. However, none had provided a systematical and standardized approach to test the Vickers hardness and reduced contact modulus through the depth-sensing indentation technique on Bi-In-Sn lead-free alloys. In this thesis, Bi57In26Sn17 was

selected as a good example of the lead-free solder alloy candidate to perform microindentation test.

The depth-sensing indentation technique is a localized technique to measure the mechanical properties of various materials. It has been greatly improved since the advent of the first “Brinell test.” Microindentation then starts to become popular, assorted indenter shapes have been derived to suite different measurement requirements. Although indenter area functions are different from one to another, the general methodologies are the same. Therefore, Vickers pyramidal indenter was employed in this thesis study. Current state-of-art depth-sensing indentation technique is nano-indentation. In comparison to micro-indentation, nano-indentation seems more advanced as nano-indentation enables testing within the nanoscale. However, fairly small indenter tip sizes and the consequential imprints are not suitable for studying the apparent properties of Bi-In-Sn alloys as the imprint sizes may only be a few micrometers or even nanometers which could be the size of individual phases of Bi-Sn-In alloy sample. So, it is of great importance to characterize the microstructure of the sample alloy to make sure the indentation imprints are much larger than average grain sizes to have the contribution from each phase. According to the requirements, microindentation technique is the most reliable method for measuring the mechanical properties for Bi-In-Sn lead-free alloy.

Unlike nano-indenter that allows one to continuously measure the contact stiffness during the indentation process, microindentation generates load-displacement curve during

indentation and requires researcher manually to obtain the contact stiffness afterward, which seemingly inconvenient. Actually, this process reduces the uncertainty of instrumental errors to a great extent. A detailed method for obtaining contact stiffness through the unloading curve will be discussed.

1.2 Thesis outline

The thesis is organized as follows: Chapter2 begins with the basics of microindentation technique along with special terms that will be used in this research, followed by the literature reviews of previous works on nano/microindentation. The circumstances that lead to the investigation of Bi-In-Sn alloy were then briefly discussed and the relative properties of Bi, In, Sn elements and their compounds were reviewed. Chapter 3 presents a series of detailed experimental procedures, including: sample preparing, initial value setting, and measurement of the contact stiffness as well as the diagonal lengths. In Chapter 4, the characterization results of the Bi57In26Sn17 alloy were given. In chapter 5, the microindentation results were presented and the indentation size effect and the creep behavior were observed from plots along with a discussion. Chapter 6 is the conclusion of the thesis.

Chapter 2 : Background

In order to explore the mechanical properties of different materials, scientists and engineers have been using indentation test since the 19th century. In 1885, Boussinesq [5] developed a method to compute stress and displacement in an elastic body loaded by a rigid axisymmetric indenter. Brinell [6] used a hard steel ball to press into a designated material surface for a specific period of time so that the imprint area left on the surface of the material could be measured: such a method was soon widely adopted for industrial use. Since the extensive use of the Brinell test, scientists and engineers have developed different indentation methods with different indenters such as the Rockwell test with a conical indenter or a Vickers test with a Vickers pyramidal shaped indenter.

2.1 Overview of the technique

The indentation technique applies a force through the indenter to press it into the polished surface of the sample material, while at the same time recording the real-time load and displacement of the indenter to generate a load-displacement curve for data analysis. Then, one can obtain the projected area of the indentation to calculate the reduced Young's modulus, hardness and other important mechanical properties.

The Nano/Micro-indentation technique has a wide application nowadays, not only being used in industrial engineering areas, but also having high scientific value; indentation tests

can be used to measure metals, alloys, semiconductors, glass, minerals and even organic materials like polymers. The mechanical properties that can be obtained through indentation tests include, but are not limited to: Young's modulus, hardness, contact stiffness, compliances, creep, elastic energy, plastic energy and fracture toughness.

Figure 1 is a schematic illustration of a typical structure of nano/micro indentation instrument.

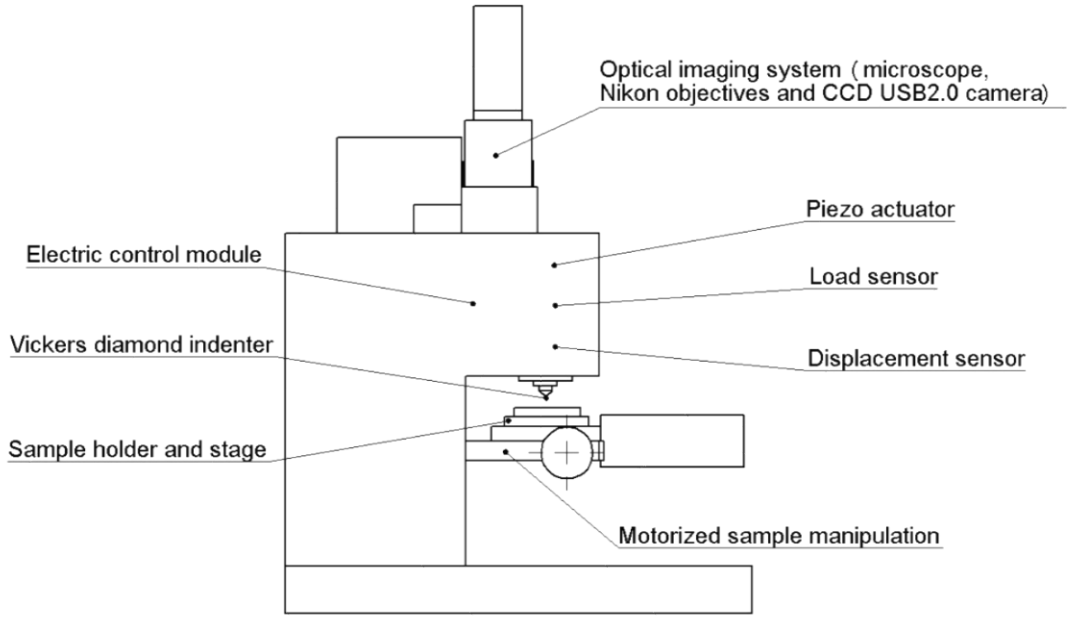

Figure 1: Schematic illustration of a micro hardness indenter

From the bottom to the top is: motorized stage; sample stage; sample holder; indenter; capacitance (works as a displacement sensor); a load sensor and a piezo actuator (used for driving the indenter into the sample surface); an optical imaging system. As the technology improves, some parts are replaceable; however, the basic structure remains unchanged.

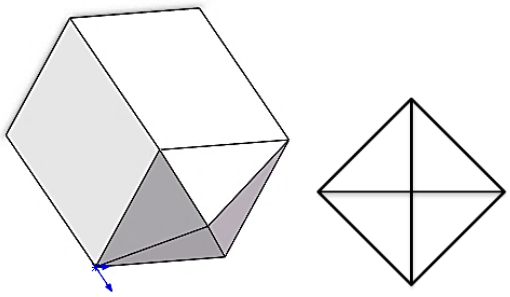

Figure 2: 3D view and top view of the Vickers hardness indenter tip

The Vickers indenter is a 4-sided pyramid indenter with a semi-vertical angle of 68° [Figure 2]. The change of projected area (A) and contact volume (V) with respect to contact depth (h) are equal to $24.504h^2$ and $8.1681h^3$ respectively. The Vickers indenter is commonly used for testing bulk materials and thin films.

During the microindentation, the indenter head is always kept in a vertical downward position, under the action of a piezo actuator, the indenter head is driven at a preset rate downwards into the surface of a sample. As the deformation occurs on the material surface, the capacitance sensor that locates in the upper part of the indenter records the real-time indenter displacement through measuring the capacitance change. After the load sensor

detects the preset-peak load, the piezo actuator starts to retrieve the indenter head from the indented material at a certain rate until the load is zero and the indenter head leaves the original surface of the material. Besides the material position adjustment, the drivable sample stage can also be used for scratch tests and pre-configure the indentation coordinates for the continuous indentation experiment.

Before the micro/nano indentation experiment, the sample material must be processed. The surface preparation may include, but is not limited to grinding, polishing, and ultrasound cleaning. The reason is to avoid an inclined surface, surface stresses, impurities and oxidations that can affect experimental results or damage the indenter head. The sample needs to be fixed on the stage, and then one can set up the initial height of the indenter and start to program the indentation parameters. When the indentation load falls back to zero, the indenter head leaves the surface of the material and stops, the indentation experiment is finished.

For the nanoindentation test, all the data is collected during the experiment process; and for the microindentation, the projected contact area requires special attention. The most important data collected during the test are the indentation load and the indenter displacement. The load-displacement curve is automatically generated.

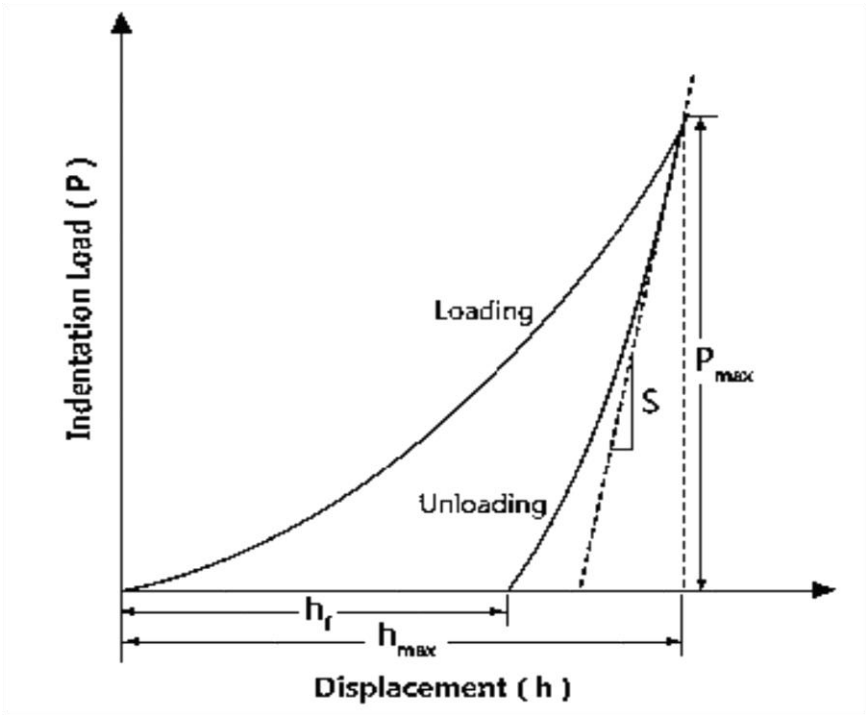

Figure 3: A typical load-displacement curve

As shown in Figure 3, the Y-axis represents the load applied by the indenter to the surface of a sample; the X-axis represents the indenter displacement. Starting from zero, the load gradually increases as the depth of the indentation increases; then the load reaches P_{max} and immediately decreases as the indenter is withdrawn from the maximum depth h_{max}. The load continuously decreases, while at the same time the depth of the indenter decreases at a rate, leaves at depth h_f and the unloading curve thus is generated.

2.2 Literature review on the indentation technique development

Sneddon [7] had derived a general relationship among the load-displacement and contact shape as

$$P = \alpha h^m \tag{1}$$

where p is the indentation load, h is the elastic displacement of the indenter, α and m are constants. (m=1 for flat cylinders, m=2 for cones m=1.5 for spheres with small displacement).

With the loading-unloading curve known, the contact stiffness (S), the plastic energy, the elastic energy and the total indentation energy can be calculated.

The contact stiffness of a material describes the ability to resist elastic deformation. It is defined as the ratio of the force to the deformation generated by the force:

$$S = \frac{dP}{dh} \tag{2}$$

In an indentation test, the contact stiffness can be understood as the ability of the material to resist indentation. Commonly, there are two ways that can be used to obtain contact stiffness through an unloading curve. The first method is through a linear fitting to a fraction

of upper 1/3 portion of the unloading curve and uses the resulted slope as an estimation of the sample's contact stiffness. However, using this method can generate errors as the number of data points selected for linear fitting is hard to decide. [8] Besides, on small load indentations, data are unstable and noises are notable and can lead to a significant deviation of the result. The second method is to use a nonlinear curve fitting to describe the power-law relation of the unloading curve as

$$P = \alpha \left(h - h_f \right)^m \tag{3}$$

where P is the indentation load, h is the total displacement, h_f represents the final depth, α and m are both constants. A data processing software like Origin or Matlab is usually employed to do the least square fitting to get the three parameters (hf, α, m) and then the stiffness can be found by differentiating F with respect to h.

Some instruments also enable the measurement of contact stiffness through "dynamic techniques", which allow continuous measurement while the test is going on.

Young's modulus is an important property that describes a material's mechanical behavior. From the macroscale point of view, E can be treated as the ability to resist elastic deformation; from the microscale point of view, E reflects the material's bonding strength between molecules, atoms or ions. However, sometimes the variation of E for one specific

material can be more than 5%, depending on chemical composition, microstructure and temperature. E is defined as stress over strain:

$$E = \frac{\sigma}{\varepsilon} = \frac{P / A}{(L' - L) / L} = \frac{PL}{(L' - L)A} \tag{4}$$

where P is the force, A is the cross area, L is the initial length, L' is the final Length.

An indenter is usually made of a material with extreme hardness, small thermal conductivity and chemical inertness. Diamond, then becomes the preferable candidate.

Hertz [9], who analyzed the elastic contact of two spherical surfaces with different radii and elastic constants, had found that the radius of the circle of contact is related to the indenter load, indenter radius and the elastic properties of the materials, which formed the basis of the later study in contact mechanics and provided reasonable explanations to include the analysis of the effect of non-rigid indenters.

The diamond indenter in most cases is treated as nearly rigid, however in practice, it is not. The non-rigidity of indenters were studied by S.Timoshenko and J.N.Goodier. [10] The elastic modulus (Ei) of a non-rigid indenter along with its Poisson's ratio (νi) according to their finding was further expressed by a so-called reduced modulus "Er" as

$$\frac{1}{E_r} = \frac{\left(1-v^2\right)}{E} + \frac{\left(1-v_i{}^2\right)}{E_i} \tag{5}$$

Sneddon [11] had developed an equation that stated the relationship between the radius of the contact circle and the indenter load for conical indenters, which was a step forward of the classic work of Hertz on the analysis of elastic contact between non-rigid spherical indenters and a flat surface. In a practical indentation testing, pyramidal indenters such as the Vickers indenter was treated as a conical indenter that gave the exact same relationship. The relationship between the total indenter displacement and the indentation load was expressed by:

$$P = \frac{2}{\pi} E_r h_{max}^2 \tan \partial \tag{6}$$

where P is the indentation load, Er, is reduced modulus, h_{max} is the maximum distance between the apex of the indenter and the original free surface of material and α is the cone semi-angle.

By further taking the derivative of load with respect to the indentation depth, an important result is reached:

$$\frac{dP}{dh} = 2\left(\frac{2}{\pi} E_r \tan \partial\right) h \tag{7}$$

It is known that the depth profile of the indenter is:

$$h = \frac{\pi}{2} a \cot \partial \tag{8}$$

Substituting Eq. (8) in Eq. (7) yields:

$$E_r = \frac{1}{2} \frac{dP}{dh} \left(\frac{\pi}{A}\right)^{\frac{1}{2}} \tag{9}$$

where the A is the projected area.

An alternative method for determining the projected contact area between the indenter and the sample surface is to use indenter area function (shape function) [12] — a function relates the cross-sectional area of the indenter with the depth after the final unloading. This method is usually employed when the imprint is too shallow to perform the traditional projected contact area measurement.

From equation (2), one knows that $\frac{dp}{dh}$ is simply the contact stiffness of the material. The projected area (A), can be further calculated from the diagonal length (D) that directly measured from the imprint after the indentation as:

$$A = (\frac{D}{\sqrt{2}})^2 \tag{10}$$

, we now obtain the equation established by Love, [13] Galin, [14] and Sneddon [11] as

$$S = (\frac{2}{\pi})^{\frac{1}{2}} D E_r \tag{11}$$

Bulychew and his co-workers [15] had conducted a series of experiments based on this equation. Pharr, Oliver, Brotzen and their co-workers [16] had further proved the validity of the equation for any indenter shapes that could be described as a body of revolution of a smooth function. A good agreement between the experimental value and the calculated value using this equation had further supported the results from the Vickers indenter (Pyramidal indenters).

The hardness measures the level of a material that resists plastic deformation. The hardness is commonly defined as an average pressure under the indenter:

$$H = \frac{P}{A} \tag{12}$$

where P is the applied load; A is the projected area of contact between the indenter and the sample.

According to Anthony C. Fischer-Cripps's book, [17] for a Vickers indenter, the Vickers diamond hardness VDH is calculated through the actual surface area of the impression, and had a relationship as shown below:

$$HV = \frac{1}{g}\frac{2P}{D^2}\sin\frac{\theta}{2} \tag{13}$$

$$HV = \frac{1}{9.80665}\frac{2P}{D^2}\sin\frac{136^\circ}{2} \tag{14}$$

$$HV = 0.1891\frac{P}{D^2} \tag{15}$$

where P is the indentation peak load, in Newton (N), D is the Diagonal length, in millimeter (mm). The equation was also employed in this thesis in calculating the hardness values of Bi57In26Sn17 lead-free alloy under different dwelling periods.

Further, with the known relation between the contact stiffness, the imprint diagonal length, the peak load, the Vickers hardness value and the reduced modulus, Oliver and Pharr [18] developed a relationship

$$E_r = \sqrt{\frac{S^2 H \pi}{4 P \beta^2}} \tag{16}$$

where β is the geometry correction factor. For the Vickers indenter, β =1.012. [17]

There are questions on the reliability of the indentation results. Doerner and Nix [19] performed a series of experiments on different materials to investigate the plastic and elastic properties. They combined many of the ideas at that time to find the hardness and the elastic modulus. They observed that during the unloading, the contact area remained unchanged. It was further confirmed and suggested by them that for some materials the upper one-third portion of the unloading curve can be used for a linear curve fitting to obtain the contact stiffness. The contact area was also suggested by them to obtain through extrapolating the initial linear portion of the unloading curve to zero load, combining with the indenter shape function. Their experiments on METGLAS2826 had showed the advantage in the accuracy for the use of the extrapolated depth rather than either the peak load depth or the final depth. However, the situation of the linear unloading curve was proven not common. Mostly, the unloading curve was better described by power laws. Besides, they employed the example of <111> silicon to show that the use of the ideal indenter geometry could result in a large over-

estimate of the hardness at small depths (the ISE effect was first identified) and they attributed the deviation to the blunter indenter tip. Oliver and Pharr [8] had done several experiments on aluminum, tungsten and soda-lime glass, fused silica, sapphire and quartz through nanoindentation with a Berkovich indenter. They performed multiple cycle loading-unloading tests under constant temperature and pressure. They observed the non-linear unloading curves for five of the tested materials, except for silicon, which only displayed the linear region near the top of the unloading curve, and showed an apparent discrepancy with the linear behavior observed by Doerner and Nix (1986). The reason of the disagreement was further explained as the steep unloading curve and the insufficient enlargement of the unloading curve. In the case of nanoindentation, Oliver and Pharr (1992) suggested an alternative way to present an analysis technique that accounted for the curvature of the unloading curve and provided a procedure for determining the depth that could be used with indenter shape function to obtain the contact area at a peak load.

Over the last few decades, with the improvement of testing equipment and numerous experiments being conducted, the testing accuracy had been greatly improved and new innovations such as nanoindentation testing of thin films and the use of finite element simulation software have been developed. The use of the nanoindenter accompanied with the real-time stiffness measurement technique has largely decreased the operational difficulties and further promoted the testing efficiencies. However, slight deviations of the input parameters had drawn great attention as it may lead to considerable quantitative error. Plastic properties obtained from the loading–unloading curves could be greatly affected by small

variations of the input parameters [20], the importance of accurate contact area estimation can be then realized. [21].

Creep usually occurs during indentation of soft metals and alloys. When creep occurs, stress exponent is used to describe the stress-dependence of the material's deformation rate:

$$\dot{\varepsilon} = A\left(\frac{\sigma}{\mathrm{E}}\right)^{n} \tag{17}$$

where σ is the stress and E is the contact modulus of the material, n is the stress exponent.

With the development of nanoindentation technique, the indentation size effect (ISE) – the decrease of the indentation hardness with increasing the indentation load at low penetration depth has attracted great interest.

Scientists [22] [23] [24] had respectively documented a strong size dependence of indentation hardness for microindentation. Using small indenters (<10μm) in single crystals or fine-grained polycrystals often results in significant ISE. The hardness difference obtained from the same material using the same indenter shape of different widths could range up to 2 to 3 times, which has been considered as a crucial element in thin film testing.

So far, scientists have come up with several possible explanations about the mechanism of the ISE [25] [26] [27] [28] [29]: the instrumental measurement limitation, the friction between two surface layers, the existence of surface layer content (asperities and dents), and the work hardening. The ISE, according to Nix and Gao's model, is related to the concept of geometrically necessary dislocations (GNDs) (Nye 1953): an inverse relationship between the GND density and the indentation depth introduces the ISE.

In microindentation study of alloys like Bi-In-Sn in this thesis, an increase of Vickers hardness with the decrease of indentation depth could be possibly encountered.

Moreover, sinking-in or pilling-up can also happen during the microindentation, which could further lead to the deviation of experimental results.

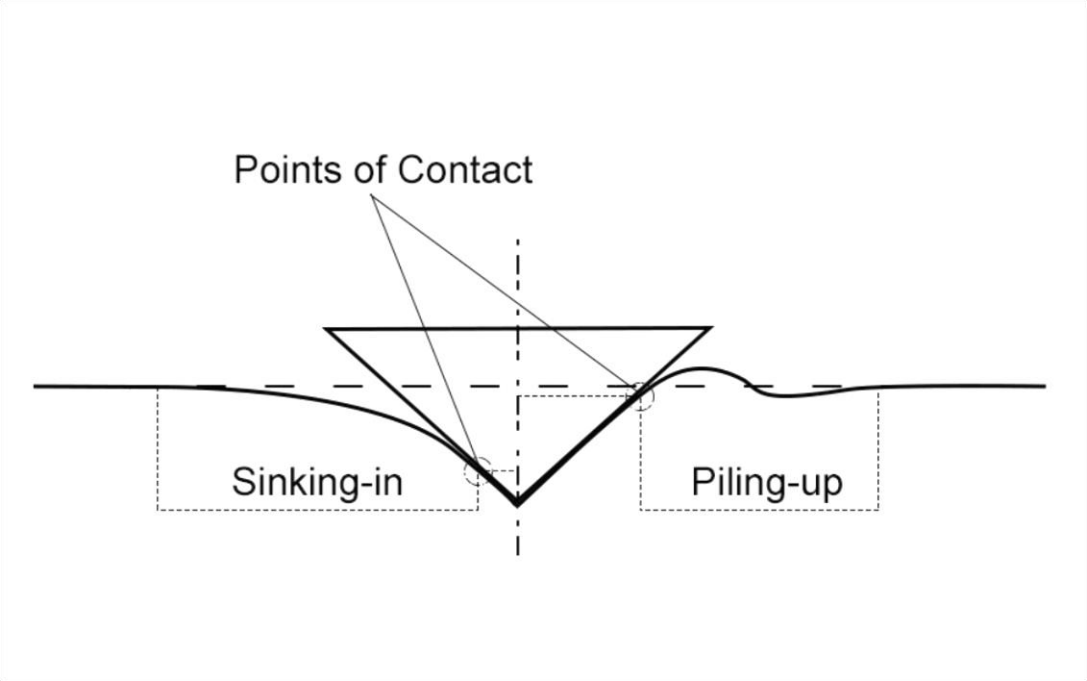

Figure 4: Schematic of sink-in and pile-up on a sample surface

As shown in Figure 4, the left side of the central line shows the Sink-in behavior, accompanied by the estimation deficiency of contact area; the other side shows the pile-up behavior, which usually results in overestimation of the contact area. Tabor [30], Oliver Pharr [16], Nix [31]and their co-workers had tried to explain this effect through the strain-hardening potential of material, and had revealed that the pile-up often occurs when materials are highly strain-hardened and the opposite situation usually occurs when materials have high strain-hardening potential. Cheng [32] used dimensional analysis and finite element calculation to derive a relationship between the indentation deformation and mechanical properties. Compared with results from Oliver-Pharr's procedure [8], they concluded that using the Oliver-Pharr method for low strain hardening potential materials may not yield accurate contact depth since the pile-up is significant. Huang and his co-workers [33] investigated

indentation on Ni-Ti shape memory alloy and observed the transition from sink-in to pile-up as the temperature increased from low to high and related the phenomenon to both strain hardening and severe plastic deformation. Other than temperature and strain-hardening, indentation depth, annealing and crystal orientation for single crystal materials were also found to have impacts on determining the pile-up and sink-in according to recent research findings.

2.3 Bi-In-Sn Alloy

Bismuth (Bi) is the No. 83 element in the periodic table and a post-transition metal, with a relative atomic mass of 208.980. Bismuth has a melting point of 520.7 °F (271.5 °C) and has a rhombohedral lattice structure with a density of 9.79 g•cm^{-3}. As the density is very close to lead density at room temperature, bismuth sometimes can be used as a replacement for lead (Pb).

Tin (Sn) is the No.50 element in the periodic table, with relative atomic mass of 118.710. The melting point of the tin is 449.47 °F (231.93 °C). β-Sn appears white in color in nature, with a body-centered tetragonal structure.α-Sn appears gray in color, with a diamond cubic crystal structure. The transformation of β-Sn to α-Sn leads to a large change of volume (24%) and formation of the tin pest [34]. The use of Sn is mainly for soldering. According to Tin Use survey 2007 [35] about half of the tin produced was used in solder in the form of an alloy with lead.

Indium (In) is the No.49 element in the periodic table. Indium appears silvery-white in color. Indium is very soft and highly ductile.

Table 1: Materials properties of pure metals

	Full name	Atomic mass	Melting point	Brinell Hardness	Young's modulus
Bi	Bismuth	208.980	520.7°F (271.5°C)	70-95(MPa)	32(GPa)
In	Indium	114.818	429.7°F (156.6°C)	8.8-10.0(MPa)	30-50(GPa)
Sn	Tin	118.70	449.5°F (231.9 °C)	50-440(MPa)	58(GPa)

Tin and bismuth forms simple eutectic alloy at 139 °C, with 57 weight% Bi and 43 weight% Sn. The equilibrium phase of Sn-Bi alloy requires 21 weight% Bi dissolved in Sn at the eutectic temperature. A small amount of α-Sn persists only at lower temperature. (<13°C)

The characterization of binary Bi-Sn system has been systematically done by researchers, through SEM (Scanning Electron Microscopy)/ EDS (Energy-Dispersive Spectrometry), DTA

(Differential Thermal Analysis)/ DSC (Differential Scanning Calorimetry) and XRD (X-Ray Diffraction) to understand the phase transitions and equilibrium. [36] [37]

The mechanical properties of Sn-Bi alloys have also been evaluated [38], and has been found to have the highest experimental ultimate tensile strength and yield strength compare to Sn–Ag and Sn–Zn alloys. Furthermore, the XRD and indentation experiments [39] revealed that the addition of indium to Bi-Sn based alloy had a negative effect on the unit cell volume of β-Sn, β-SnBi and $InSn_{19}$ phases, which might contribute to the increase of the material's elastic modulus and provide a better creep resistance.

Bismuth57-Indium26-Tin17 is a low-melt alloy, also known as fusible alloy [40] due to its low melting point (< 212°F) and lead-free specialty. Bi-Sn-In alloys were developed in 1975 by Murabayashi et al [41] as a new sealing material that provides excellent sealing property and oxidation resistance. Bi-In-Sn alloy has versatile industrial applications. Such as work holding for delicate parts, airplane application, fire protection for pressure tank, electroforming mandrels, soldering, blocking for radiation therapy. The wide range of application has allowed the material to continue to attract more and more attention since 1980's. However, current research in Bi-Sn-In alloys still could not meet the growing demand of lead-free alloy from microelectronics and other industrial applications in a short period of time. The search for the new lead-free electronic solders had been going on for decades, E. P. Wood and K. L. Nimmo [42] first reported their summaries of the issues, associated with

availability, cost, and toxicity. They also reported that the single-phase microstructures were observed from Bi-Sn-In alloys that may contribute to a good fatigue resistance.

Seung et al [43] investigated the phase diagram for Bi-In-Sn alloy through thermochemical calculation and a series of experimental works. They studied the composition of Bi-In-Sn alloy following the steps of H. Kabassis and J. W. Rutter [44]. They also verified and updated previous findings with a non-binary nature of the Sn-BiIn and Sn-$BiIn_2$ quasi-binaries and nine invariant reactions, including one eutectic, six peritectic and two peritectoid systems. Besides, an updated version of the composition triangle of the liquidus projection for Sn-Bi-In alloy had been reported along with the isothermal phase diagram near the peritectic temperature (77.9℃) as shown in Figure 5.

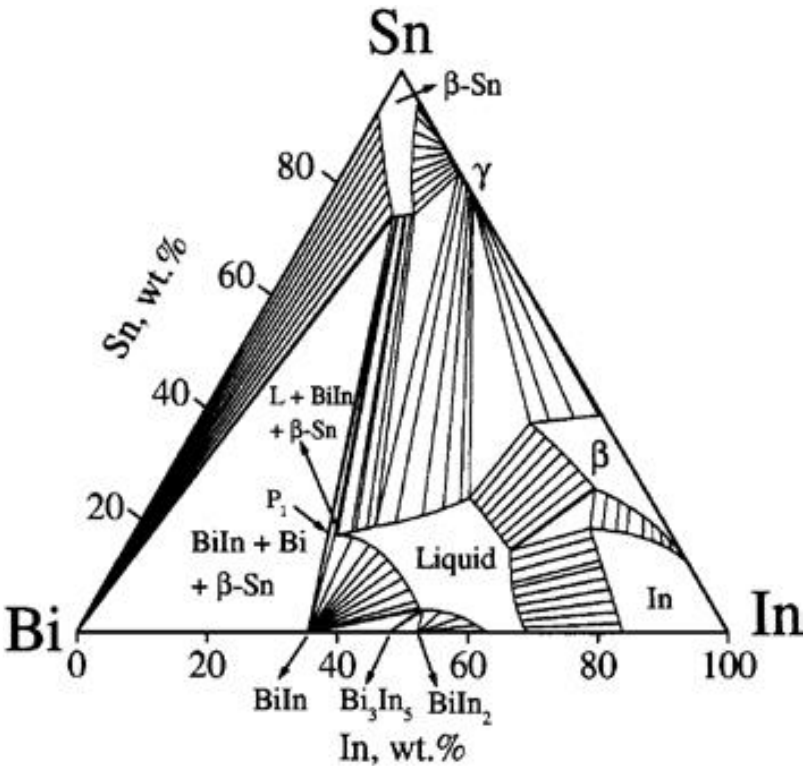

Figure 5: Isothermal phase diagram, temperature slightly below 77.9 ℃

In the report, peritectic reaction: β-Sn + Bi + BiIn was found at 77.9 °C for Bi52.92-In29.92-Sn17.6, which coincides with Scherpereel and Peretti's [45] result of the same peritectic reaction with a slightly different composition of Bi57.2-In24.8-Sn18.0. (Both have similar compositions to the sample used in this indentation study.)

The creep behavior of Sn-based lead-free solder alloys have been observed during indentation tests and has been considered as a crucial factor that could potentially affect the product serving life. The study of the indentation creep behavior has been reported by R.Mahmudi and his co-workers [46] through long time Vickers indentation test, following the

ideas brought up by S. N. Chu and J. C. M. Li [47]. Sargent and Ashby model [48] of the steady-state power law creep relationship was also employed for determining the stress exponents and the activation energies for both cast and wrought materials. Further, they also proposed a dominant creep mechanism: the dislocation creep was preferred by coarse grains and low volume fraction of second-phase particles for cast alloy, and the grain boundary diffusion was preferred by fine-grained wrought alloy with a high volume fraction of precipitated phase.

An efficient method which combines indentation constant strain rate (CSR) test with post-indent microstructural analysis through the backscatter electron images had also been used for the investigation of creep deformation by L. Shen et al [49] [50]. The eutectic Sn-Bi (Sn-57Bi) was reported with the lowest creep resistance among all tested Sn-Bi alloys (Bi concentration ranges from 3% to 100%, and the stress ranges from 90 to 450 MPa). The dominant mechanism for the creep deformation at high, intermediate and low stress region were identified as dislocation glide, dislocation climb and phase boundary sliding, respectively. Furthermore, in the test of eutectic Sn-Bi alloy, the stress exponent of n= 5.20 was found at a high strain rate region (>2×10−3/s) and n= 2.35 was found at low strain rate region (< 2×10−3/s) where the two results indicate that the dominating mechanisms in the two cases were dislocation climb with moderate phase boundary sliding and grain boundary sliding, respectively.

Studies regarding to the thermodynamic, mechanical and electrochemical properties of the Sn-Bi based lead-free ternary solder alloys (Such as Bi-Sn-In, Bi-Sn-Zn and Bi-Sn-Ag) had also been conducted by material specialists [51] [52] [53]. Bi-Sn-In among Bi-Sn based ternary phase alloy exhibits relatively good creep resistance [4], fatigue resistance [54] and oxidation resistance [55], which show good potential in the microelectronic industry. Bi57-In26-Sn17 is a candidate of the Bi-Sn-In ternary alloy family, and it is very likely to be used as a solder alloy and may display good characteristics.

Given all that, the microindentation test of Bi57-Sn17-In26 is the very first step to investigate the deformation behavior of Bi57-Sn17-In26 bulk material. The relationship between contact stiffness, diagonal length and the reduced young's modulus is employed in the calculation of reduced modulus.

Chapter 3 : Experimental Procedure

The microindentation of Bi57In26Sn17 lead-free alloy consists of 4 major steps: sample preparing, indenting, measurement, and data analysis. Special attention should be paid on the first and the last step, since in “step 1” smooth and leveled surface must be ensured in order to make sure that the indenter tip always stays away from sample surface while moving the stage; in “step 4”, the data points masked from the initial unloading points will determine the final linear fitting result. In addition, the estimation of the projected contact area has always been a difficult point for decades, unlike nanoindentation, a relatively large indentation load was chosen for this fusible alloy. As a result, projected contact area is considerably large, so one can measure the diagonal length with ease and it is less likely to generate large measurement error.

The procedure for micro-indentation of Bi57In26Sn17 alloy is described in Figure 6.

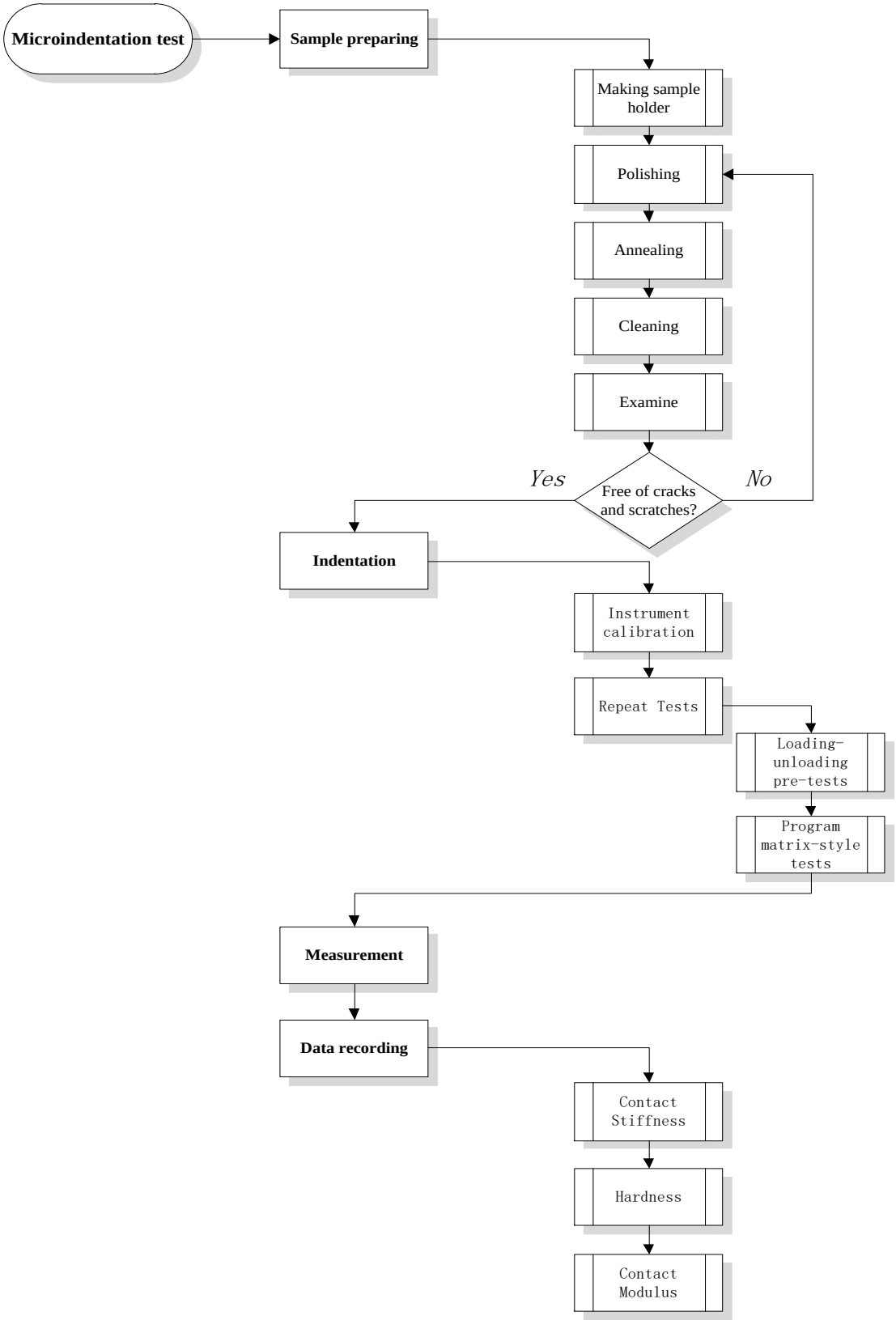

Figure 6: Experimental flow chart for the indentation of the Bi57In26Sn17 lead-free sample alloy

3.1 Sample preparation

The Bi57In26Sn17 sample used in this study was from Bolton Metal Products Co., the commercial name of the sample is Bolton 174 [56].

The samples [Figure 7] were firstly shaped into about 1.2cm×1.2cm×0.5cm, and then submerged into a prepared resin adhesive, let the system rest for 24 hours for a completely dry out to form “rigid” sample mounts. The samples were held in position against the sandpaper to perform grinding under flowing water, sandpaper of P400, P800 and P1200 micro-grits were used in sequence during the grinding. 0.5μm Aluminum oxide power was used in the polishing on a woolen polish disk. After the polishing, the microstructure of the alloys were examined under both the optical and electron microscope to ensure good surface quality. The samples were then annealed in the furnace at 50 °C (≈63% T_{melt}) for 9 hours, and cooled down at room temperature. The samples were then cleaned ultrasonically and then air dried. Lastly, the samples were examined again under an optical microscope to make sure the preparation of the good surface.

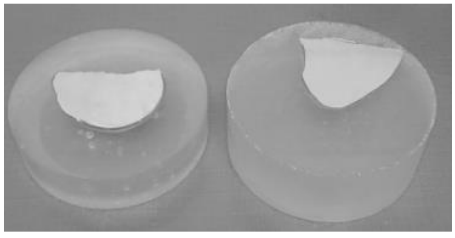

Figure 7: Image of two prepared samples

3.2 Indentation test

The indentation test was strictly performed according to the User's manual of CSM instruments [57]. Loading-unloading pre-tests were performed and had been examined under an optical microscope to estimate the effective distance between each imprint. The formal loading-unloading indentation was programed to indent in matrix form [Figure 8]. The peak load ranged from 100mN to 1000mN, and the holding times for each load condition was set from 10 seconds to 60 seconds to examine the indentation creep effect. Each test for specific loading and holding conditions was repeated for 6 times: the first indent was not counted since a small indent was left during the indenter depth adjustment process. Total 360 indentations were performed.

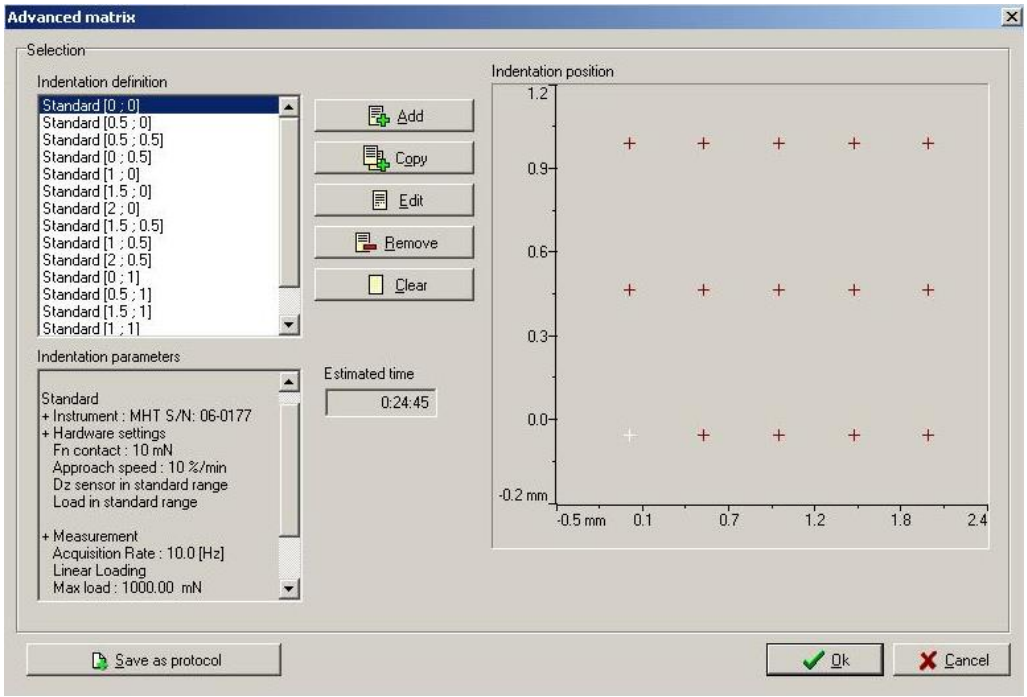

Figure 8: Indentation preset panel for a matrix test

3.3 Measurement

During unloading, plastic deformation caused by stress concentration at the edges of the indenter imprint will be permanently marked, in the case of Vickers indenter, the diagonal of the projected area would be used for calculating the contact area. Multiple measurements of diagonal lengths were performed after the indentation test. Two diagonal lengths were measured for each indent, and then were averaged [Figure 9].

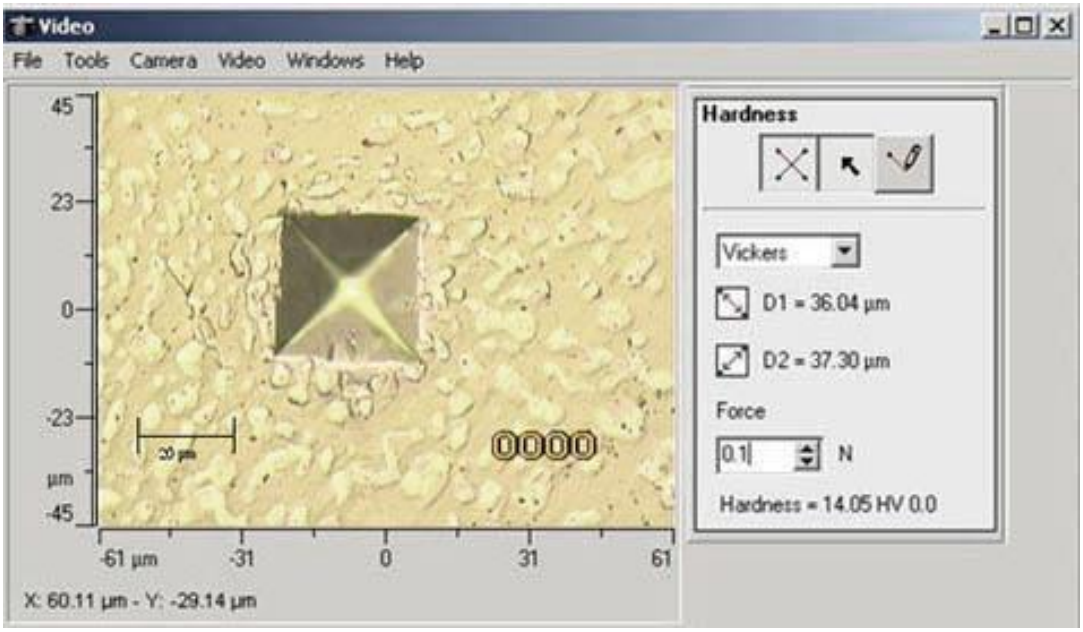

Figure 9: Measurement of the diagonal length

3.4 Data recording

Test results were saved and processed through Origin [58]. Data were firstly plotted into loading-unloading curves [Figure 10], then linear fitting was used to find the slopes for the upper portion of unloading curves. The resulted slopes represent the indentation stiffness of the material. From the stiffness, the hardness and contact modulus for each indentation were calculated. One should keep in mind that for a small dwelling period, a proper mask was needed for the initial unloading data [Figure 11], to reduce the error [Figure 12] on the stiffness evaluation.

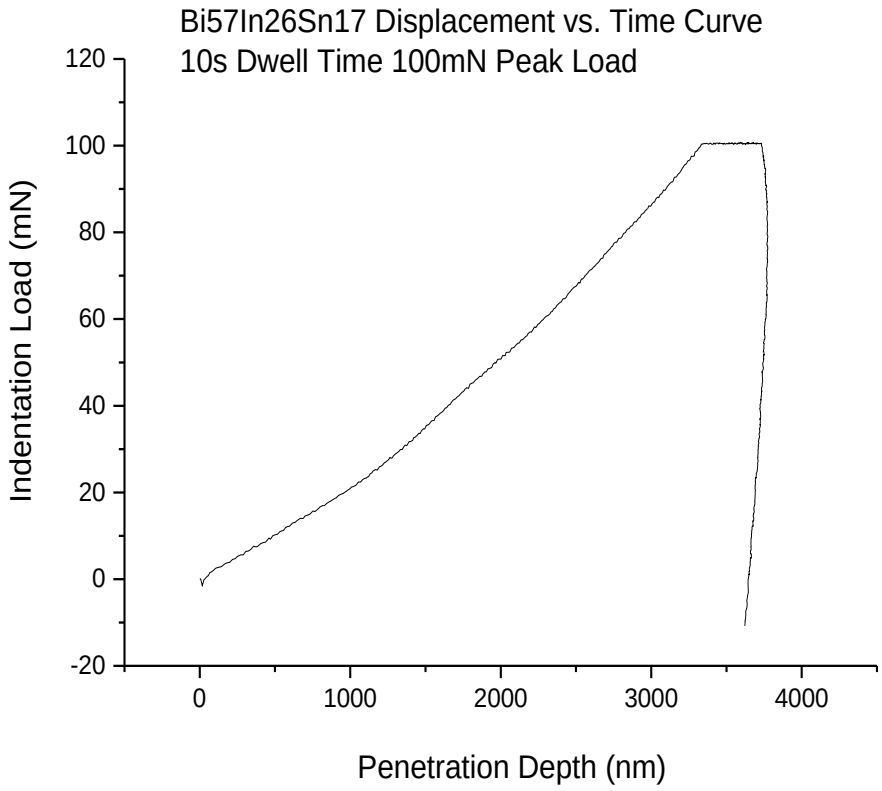

Figure 10: A typical loading-unloading curve

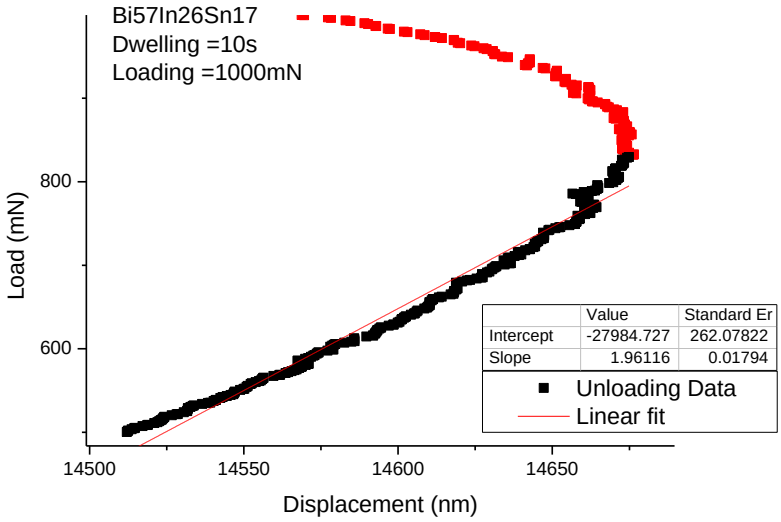

Figure 11: Unloading data with the data mask

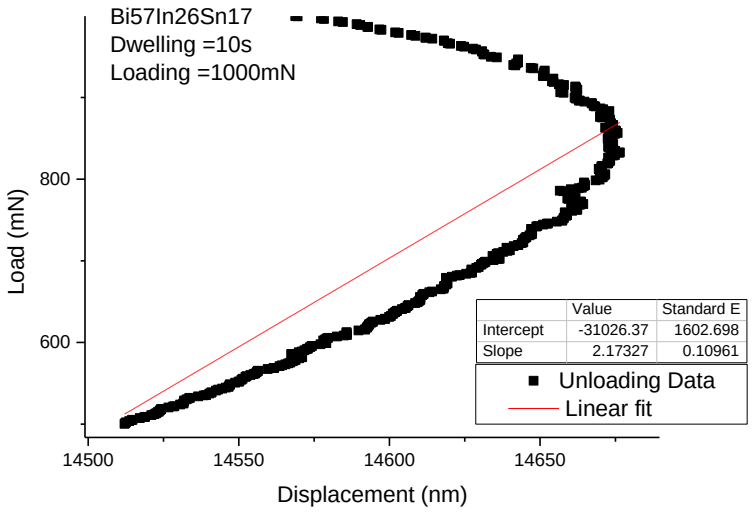

Figure 12: Unloading data without the data mask

Chapter 4 :Pre-indentation test results

This chapter begins with the composition analysis obtained from the energy-dispersive X-ray spectroscopy, and then followed by the optical microscope examinations. For Bi52.92In29.92Sn17.6 alloy at 77.9°C, there is peritectic reaction: β-Sn + Bi + BiIn [59] [60] [61]. To further confirm that the sample grain sizes were small enough to allow micro scale indenter to test the average property from these phases, the microstructure of Bi57In26Sn17 alloy was examined under higher magnification. The microstructure of the Bi57In26Sn17 alloy was also compared before and after annealing (being slowly cooled) under lower magnification.

4.1 Energy-dispersive X-ray spectroscopy result

Figure 13 shows an SEM image of the Bi57In26Sn17 lead-free alloy. In order to evaluate the homogeneity, the composition of the sample alloy at Spectrum 7 is shown in Table 1. The weight percent ratio of Bi: In: Sn is 49.69 : 22.93 : 27.38. The unit length is 10μm, and the diagonal length of spectrum 7 is between 10 to 12μm. Comparing with the ratio of 57: 26: 17, there is a moderate difference in the sample alloy for a relatively small region.

Figure 14 shows a group of the element maps from the EDX spectroscopy analysis. From the image 1, two identifiable shapes were used as reference. The bright white that scatters all over the 2nd, 3rd and the 4th image represent the detection of X-Rays on specific frequencies

that corresponding to the element. From the 2nd image, the bright flakes were distributed throughout the 2nd image. From the 3rd image, the element was largely found distributed between the interspace of the two identifiable shapes, only a few counts were detected within the region of the identifiable shapes. From the 4th image, in comparison with the image 1, the element was found largely distributed among the interspace between the two identifiable shapes. Given all that, Indium was found well-distributed in the alloy, whereas the distribution of bismuth and tin in the element map preferably compensates each other.

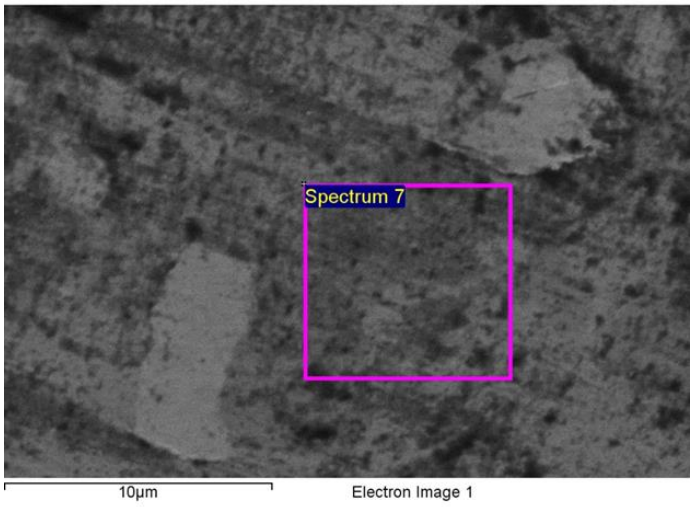

Figure 13: SEM image of Bi57In26Sn17 lead-free alloy

Table 2: Composition analysis result from EDX (Energy-dispersive X-ray) spectroscopy

Element	Weight%	Atomic%
In L	22.93	29.87
Sn L	27.38	34.55
Bi M	49.69	35.58
Totals	100.00	

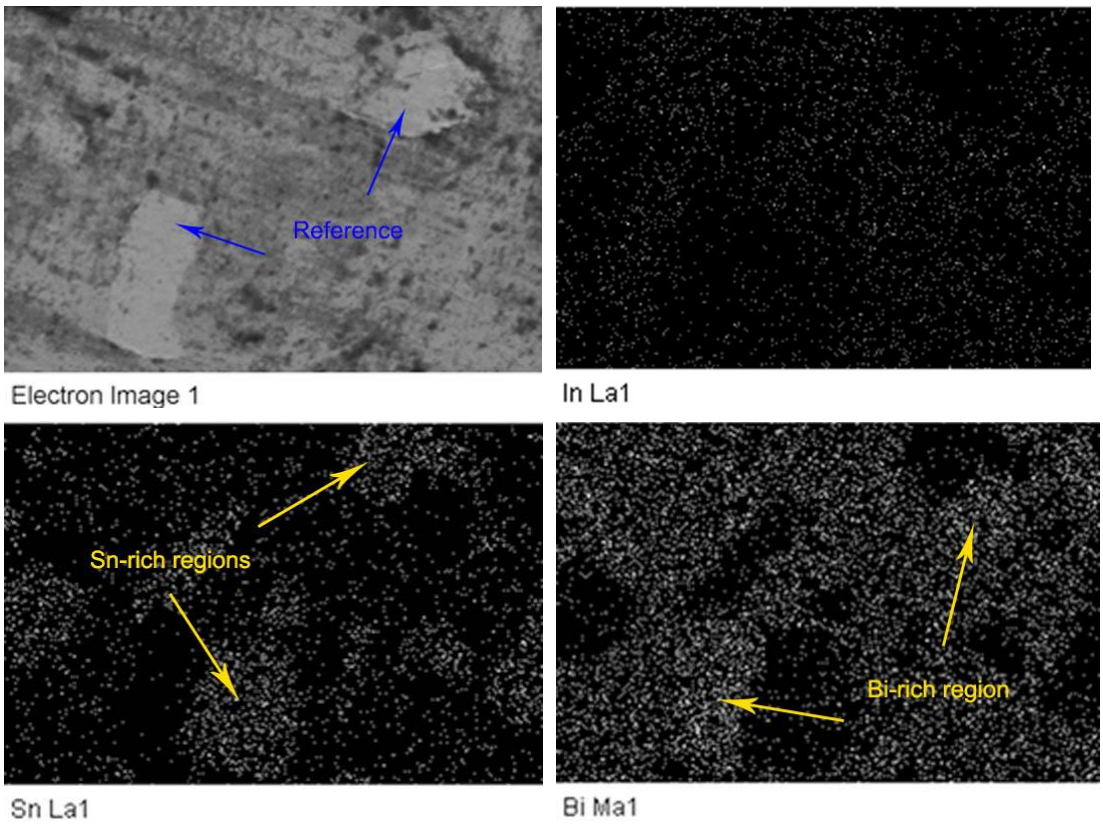

Figure 14: A group of the element maps obtained from EDX analysis

4.2 Optical microscope results

The microstructures of the samples were examined through a Nikon optical microscope both before and after the annealing. Figure 15 shows the optical micrograph for Bi57In26Sn17 alloy before annealing at a magnification of 20. The highlighted shapes formed paralleled double lines, and were partially linked, meanwhile, groups of paralleled double lines formed zigzag patterns. Figure 16 shows an optical micrograph of the same Bi57Sn17In26 alloy sample after 9 hours annealing at 50 °C with the same magnification of 20. Instead of paralleled double lines and zigzag patterns, the highlighted pattern shows comb-like irregular patterns or single sided fir-tree patterns. Figure 17 shows the same sample after 9 hours annealing under higher magnification. The pattern tends to have a specific orientation. The average width of the pattern (Bi-phase) is about 1μm, and the length ranges from 0.5 to about 5μm.

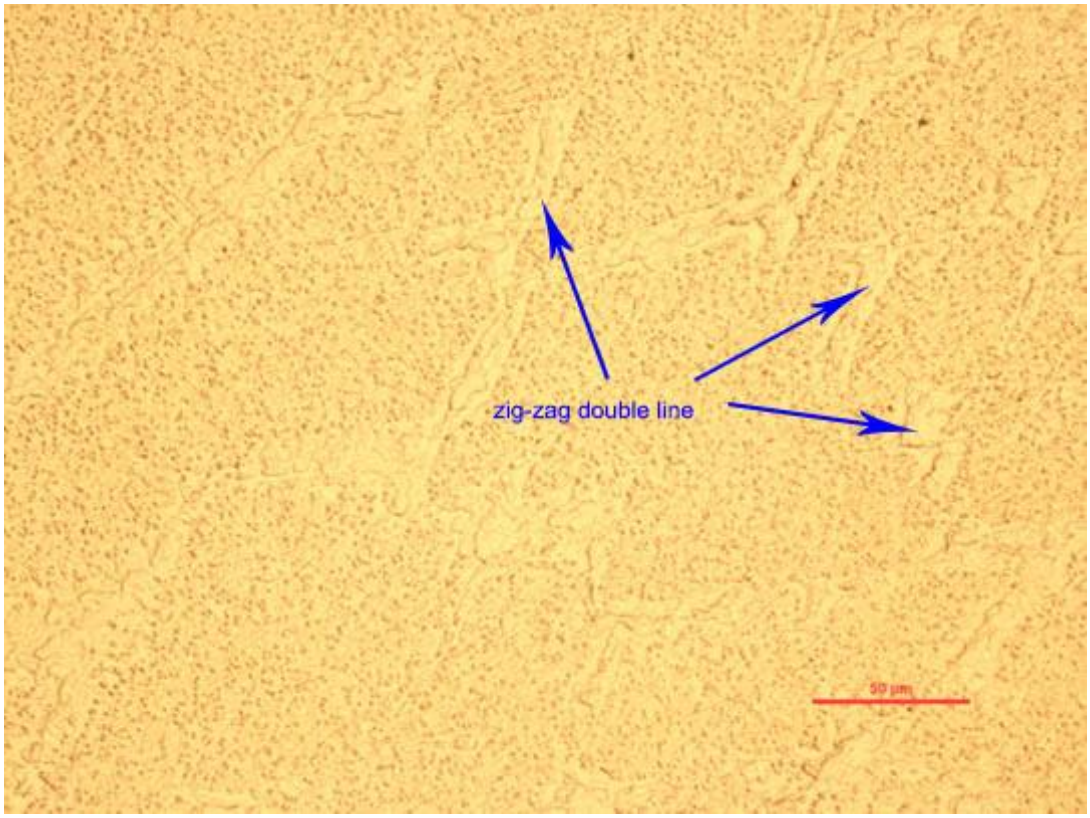

Figure 15: Optical micrograph of Bi57In26Sn17, M = 20, unit length: 50 micrometer

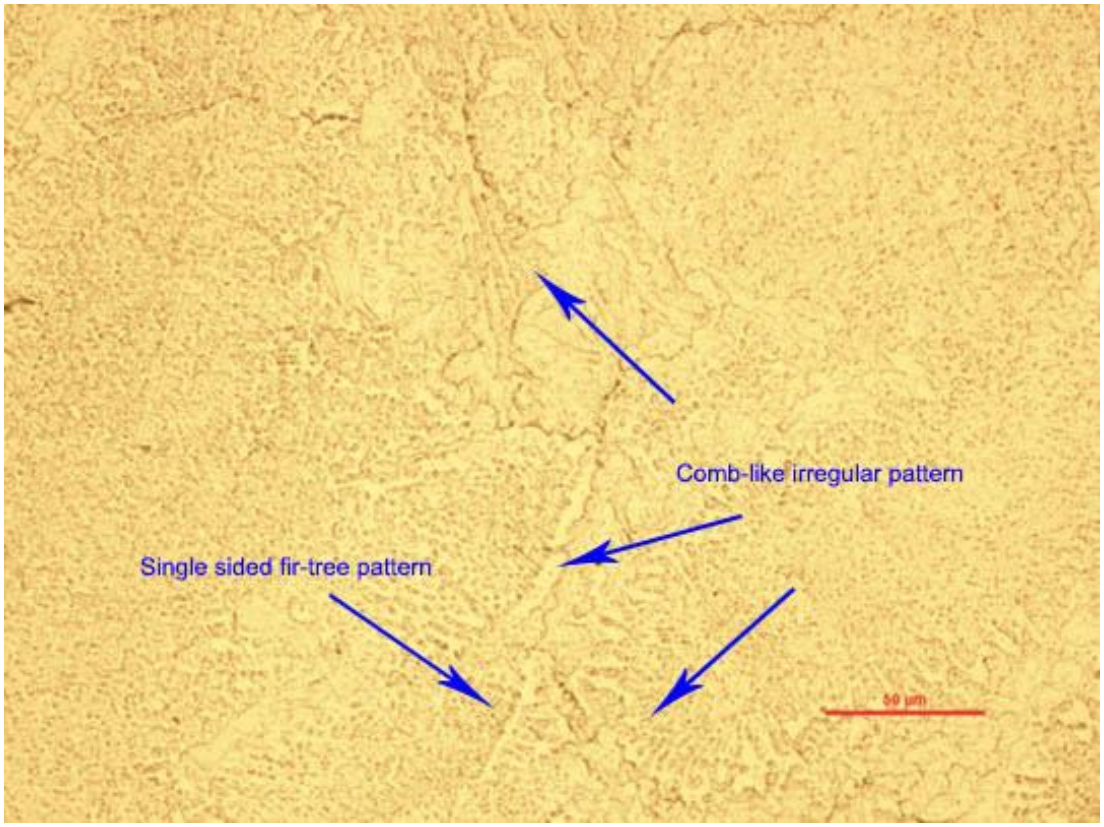

Figure 16: Optical micrograph of Bi57In26Sn17 after annealing for 9 hours at 50°C, M = 20, unit length: 50 micrometer

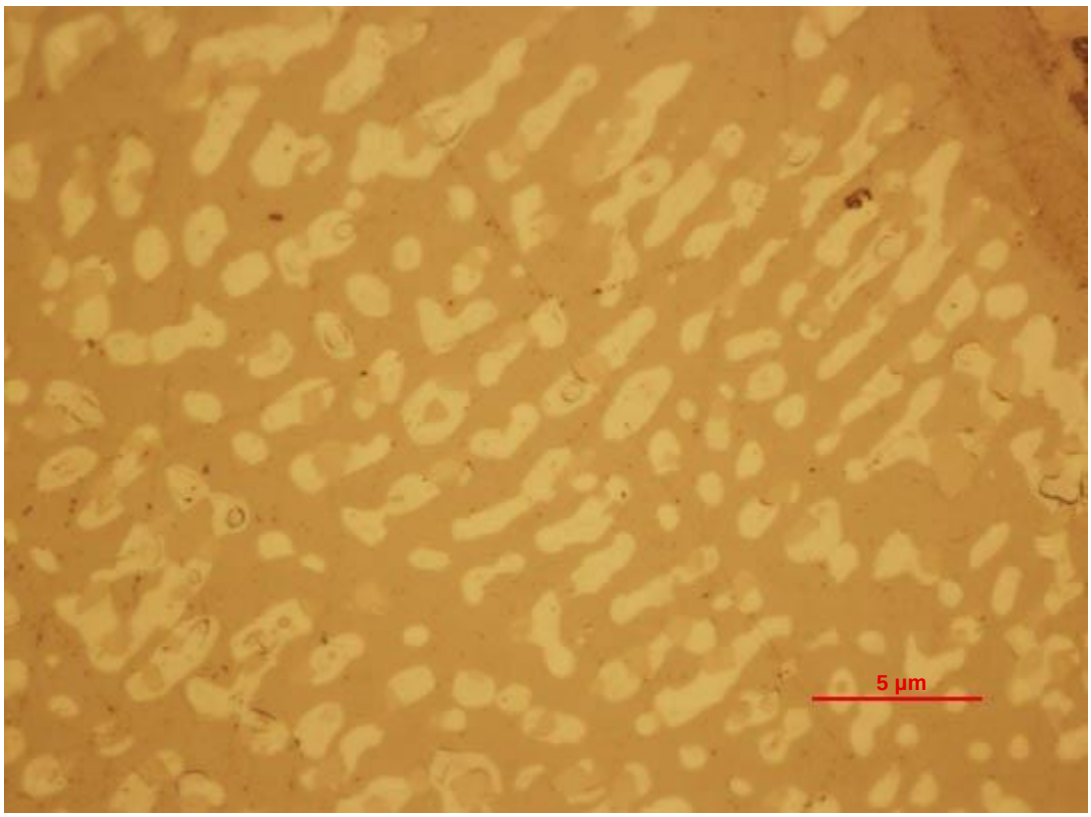

Figure 17: An enlarged view of the optical micrograph of Bi57In26Sn17 after annealing for 9 hours at 50 °C, M = 200, unit length: 5 micrometer

Chapter 5 :Indentation results and discussion

5.1 Schematics of Load-Depth Curves

A load vs. depth plot directly reflects a material's behavior during the indentation. Although some errors might be generated from an instrument and material perspective, the total errors should not exceed a specific range. By comparing the curves, one can identify the validity for a single indentation. Typical examples for the load-displacement plot for Bi57In26Sn17 lead-free alloy are shown below.

Figure 18 shows the "3-stage" loading-dwelling-unloading curves. The dwelling period was 40 seconds, the peak-load conditions ranged from 100mN to 1000mN. From the figure, ten indentation curves running from the same origin, but become slightly staggered during stage 1 when the changes of the depths of the indenter start to accumulate. One might also notice that the distance between the two adjacent unloading curves appeared to decrease as peak load increased from 100-1000mN. The resulted decrement was due to the joint action of the decrement of displacement requested to reach the max load during stage 1 and the increment of displacement during stage 2.

Figure 19 shows the comparison of the unloading curves for different dwelling periods. The indentation peak load was 1000mN. It should be pointed out that for 10s dwelling period, it was relatively difficult to obtain contact stiffness from the upper portion of the unloading

curve. The bulging out of the unloading curve at a small dwelling period condition suggesting insufficient dwelling time.

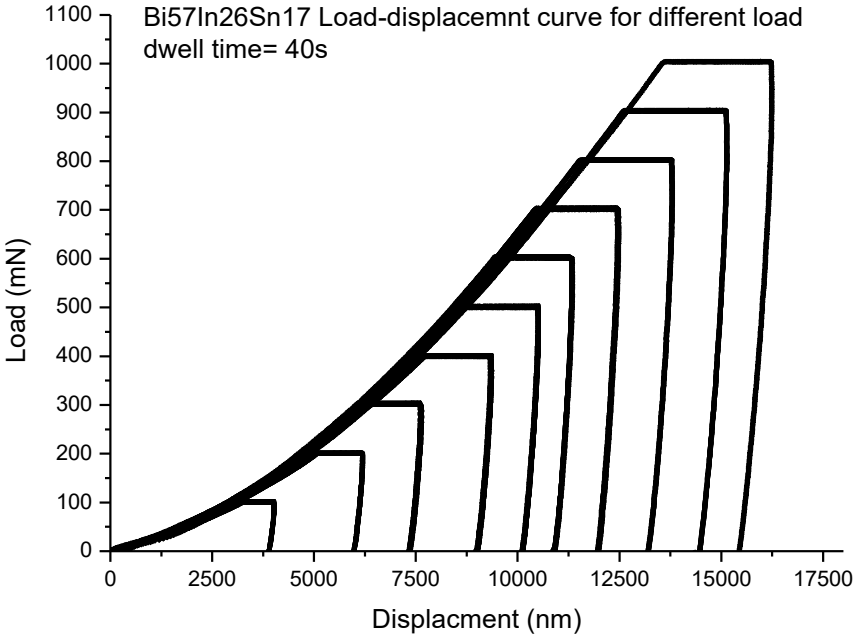

Figure 18: 3-stage loading-dwelling-unloading curves (a)

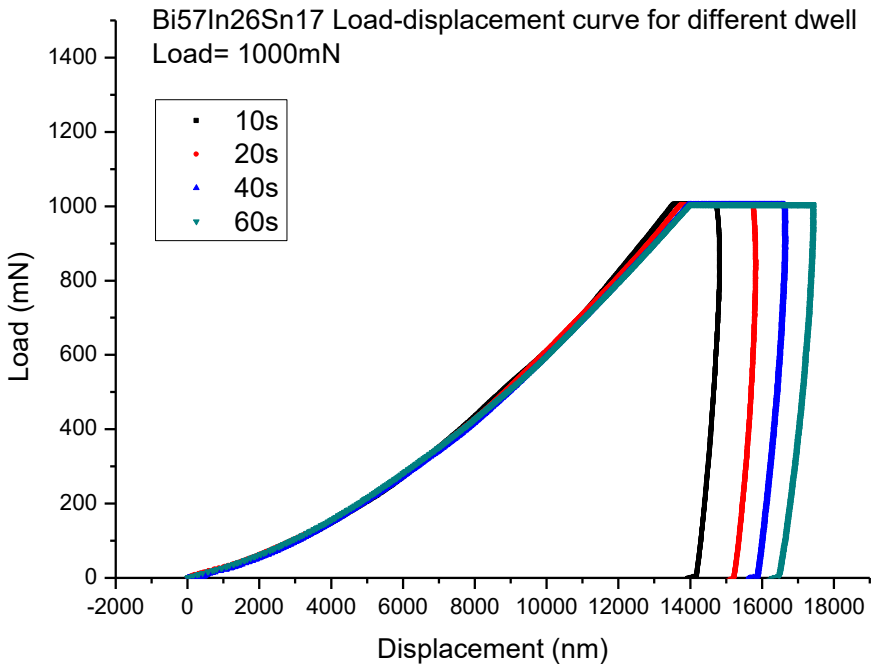

Figure 19: 3-stage loading-dwelling-unloading curves (b)

5.2 Diagonal length-load

As stated in the previous session, the diagonal length of an indent was used to calculate the Vickers hardness and contact modulus. Figure 20 depicts the diagonal length versus the indentation peak load for Bi57In26Sn17 alloy with the dwelling period varies from 20 s to 60 s. The smallest indent diagonal length was 36μm at 100mN indentation peak load, 20 s dwell period, and up to 128μm at 1000mN indentation peak load and 60 s dwell period. From the figure, the diagonal lengths increase with increasing the peak load and dwelling period. However, it should be pointed out that the diagonal length does not exhibit linear dependence on the peak load.

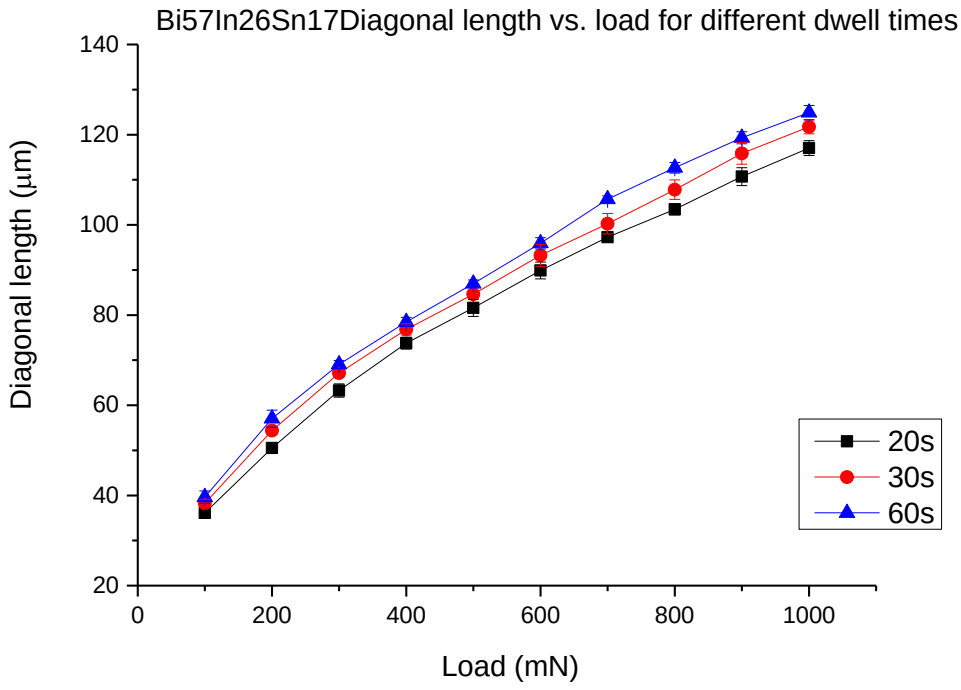

Figure 20: Dependence of the imprint diagonal length on different indentation load

5.3 Penetration depth versus dwell times

The penetration depth refers to the indenter displacement during its dwelling period. The indentation was performed using 1000mN, 600mN and 200mN peak loads, and held for different times ranging from 10 s to 60 s. The test was intended to take a closer look at the material behavior during stage 2.

Figure 21 is a linked scatter plot. For the same dwell times, as the peak load increases, the penetration depth increases. All three of the curves showed an incremental penetration depth trend as the dwell time increases. One might notice, however, that the penetration depth

does not increase linearly with the dwelling period as expected. The increasing rate of the penetration depth had a drop starting at 20 s dwell time and became minimal at 30 s dwell time, which indicates that the strain rate decreases with the prolonged dwelling period. After 40s dwell time, the penetration depth shows linear increase. The linear relationship between the penetration depth and the dwelling period can be further investigated by re-plotting the figure 22 into the log-log form, as shown in figure 23.

Figure 22 shows two segments and the breaking point is located on a nature log of 3.6 seconds of the dwell time. The first segment refers to the initial stage of the plastic deformation, and the second segment is the secondary stage of the deformation. Based on this assumption, the strain rate for the second segment can be evaluated through the linear fitting. The resulting slopes of the second stage strain rates are 5.18, 5.02 and 5.20 for 200mN, 600mN and 1000mN peak loads respectively.

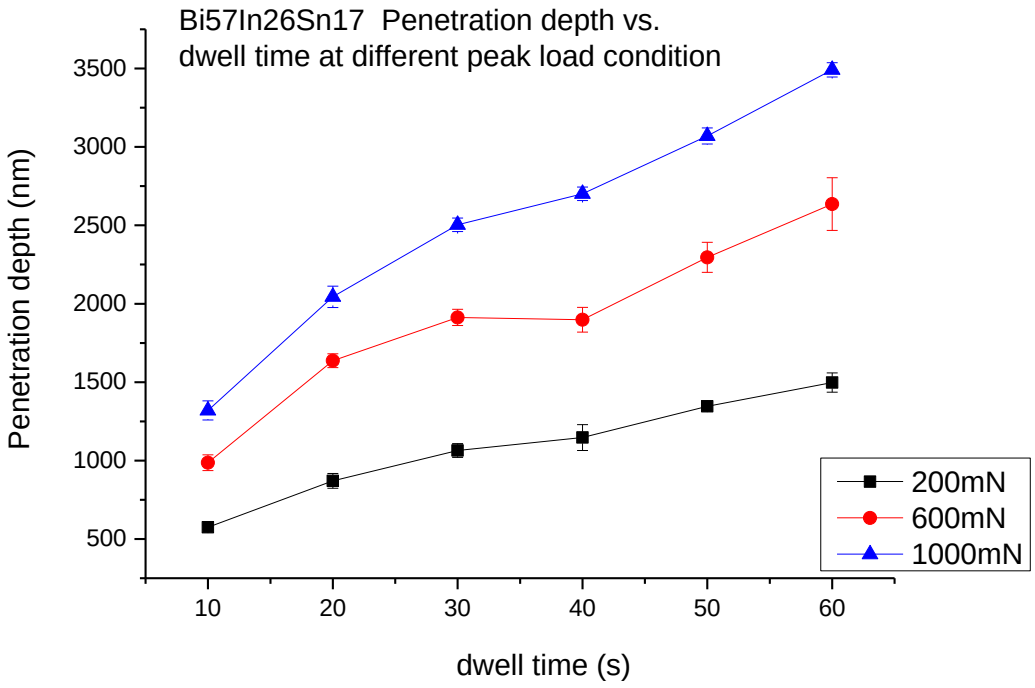

Figure 21: Dependence of the penetration depth on dwell times for different indentation peak loads

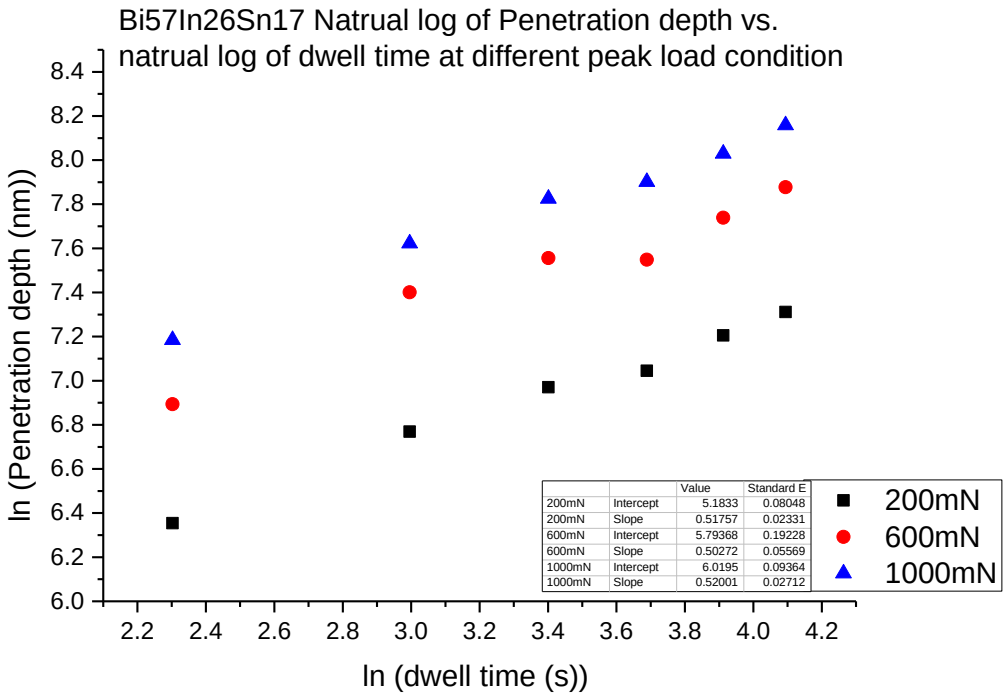

Figure 22: Dependence of the penetration depth on dwell time for different indentation peak loads in ln-ln plot

5.4 HV vs. penetration depth

Figure 23 shows the dependence of the Vickers hardness on the indenter penetration depth for 100mN to 1000mN and 10 s to 60 s dwelling time. The highest hardness value is 15.6GPa. As the indenter penetration depth increases, the hardness value decreases. This phenomenon suggests that there exists an indentation size effect (ISE). The ISE, according to Nix and Gao's model, is related to the concept of geometrically necessary dislocations (GNDs) (Nye 1953), an inverse relationship between the GND density and the indentation

depth causes the ISE. In addition, the surface hardening that gain from mechanical polishing is also considered an important factor that causes the ISE.

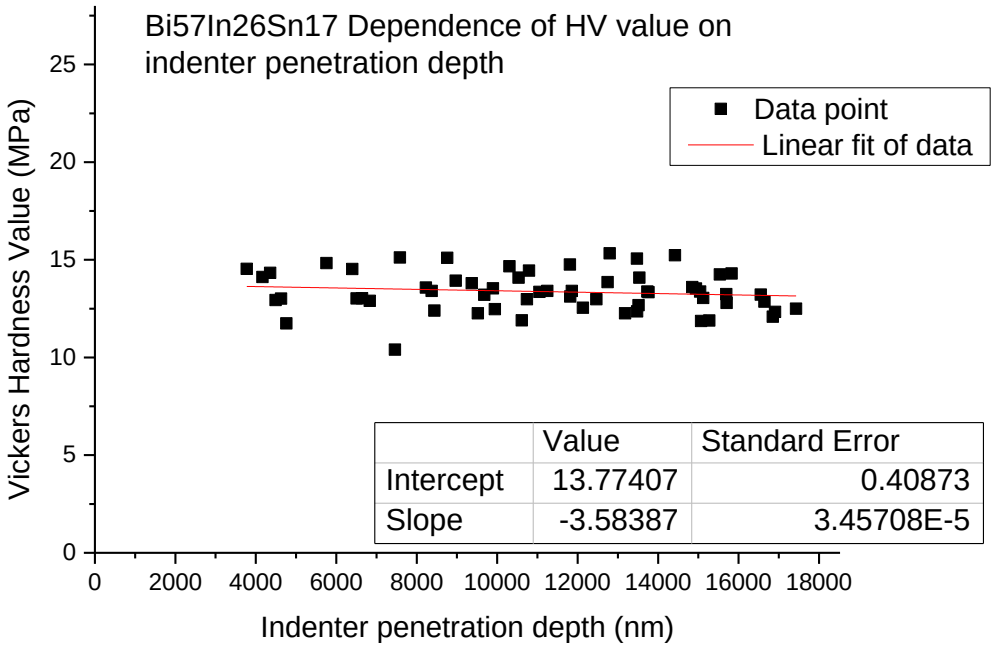

Figure 23: Dependence of Vickers hardness on the indenter penetration depth with linear fitting result

5.5 Hardness curve

Figure 24 shows the hardness result from microindentation tests at different loadings with 3 comparative dwelling periods. Hardness value is relatively steady with increasing the indentation load. In addition, 20 s group subjected to the shortest dwelling period attains

highest hardness result, when the dwelling period is extended to 60 s, the hardness value decreases from 14.5GPa at 20 s dwelling to about 12GPa.

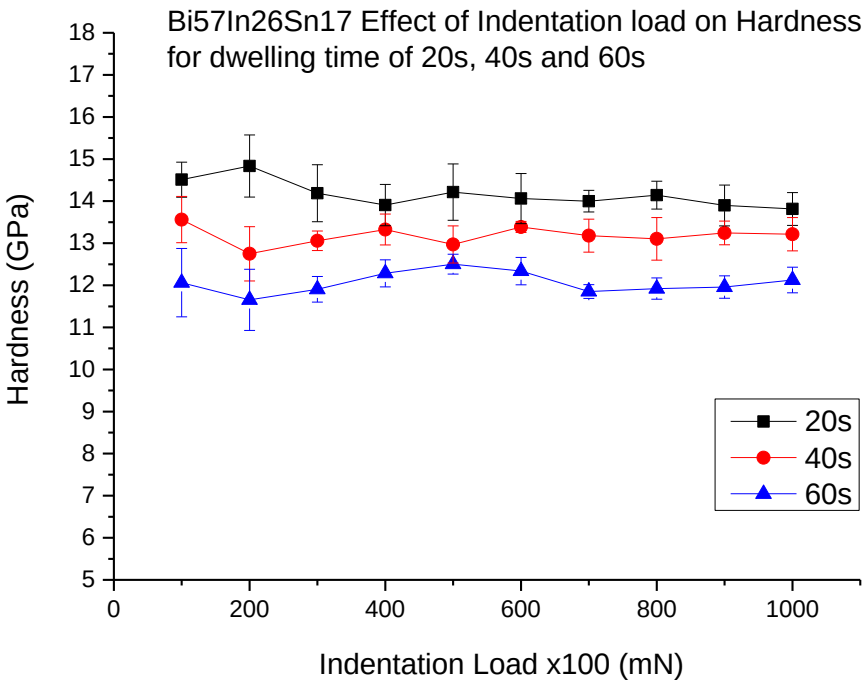

Figure 24: Vickers hardness value versus indentation load

5.6 Reduced modulus – load curve

Figure 25 shows the dependence of reduced modulus on indentation load for different dwelling periods. The contact modulus is obtained from linear fitting of the unloading curves. The contact modulus begins with relatively large deviation of 320GPa, 235GPa and 270GPa for the dwelling period of 20 s, 30 s and 60 s for small indentation load and then gradually converge at around 220GPa from 700mN of the indentation load.

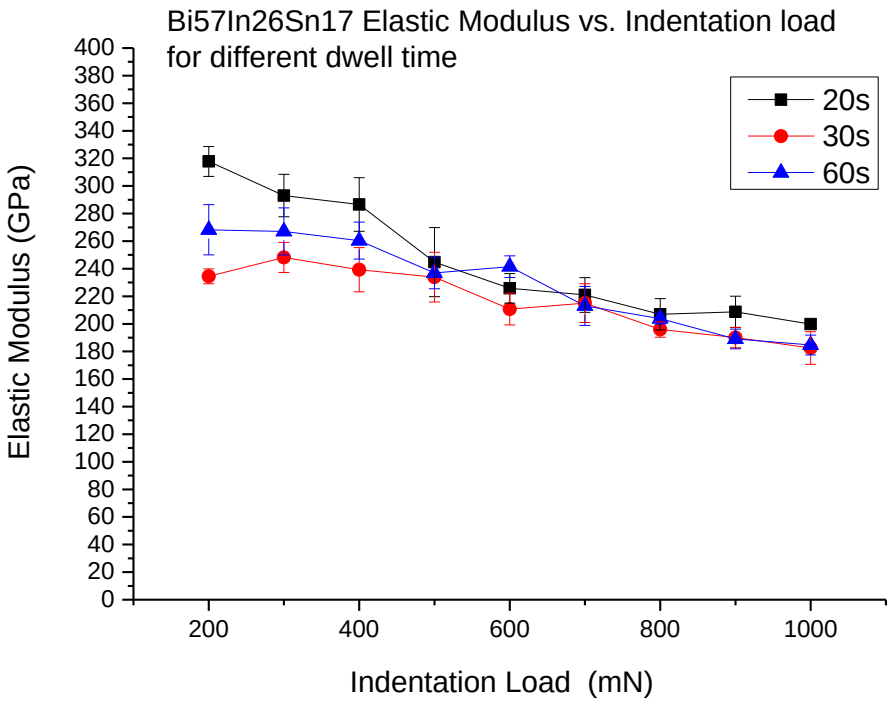

Figure 25: Load dependence of contact modulus for different dwell times

5.7 Reduced modulus – dwelling time curve

Figure 26 shows the dependence of the contact modulus on the dwelling time for the indentation of Bi57In26Sn17 sample at different indentation loads. This plot further proves the steadiness of the data at the indentation load larger than 700mN, and according to Oliver-Pharr's model, the contact moduli decrease with increasing dwelling time and finally converge to a relatively constant value.

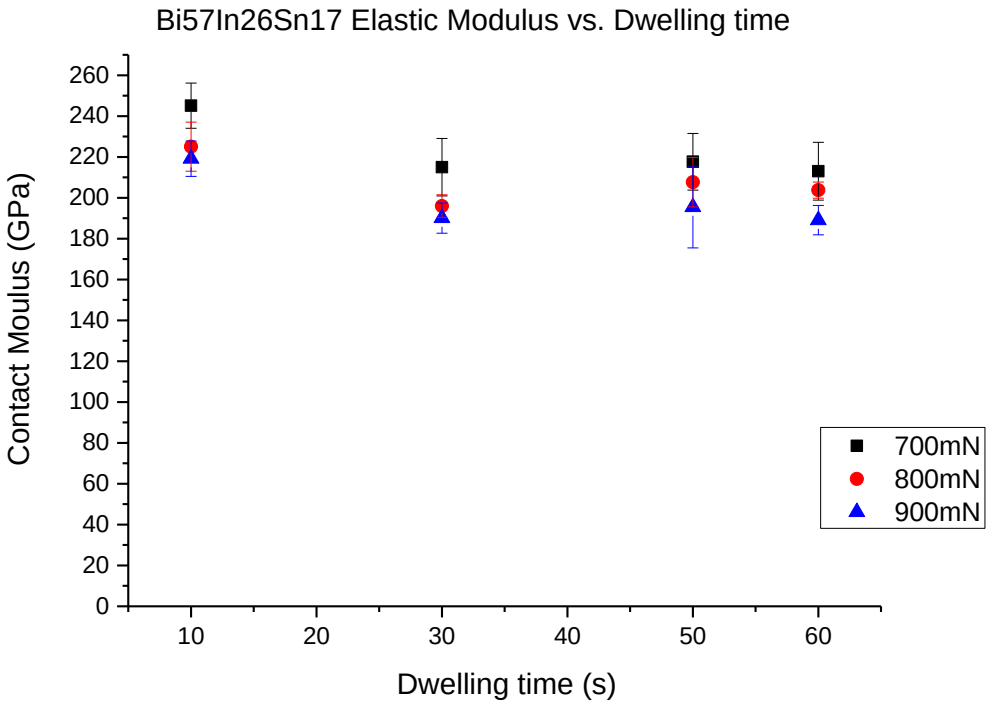

Figure 26: Time dependence of contact modulus for different indentation loads

5.8 Representation of plastic energy and elastic energy

It is known that the energy is stored and dissipated in the sample alloy during the microindentation process. The total energy (Et) change can be calculated by integration:

$$E_t = \int_0^{h_{max}} pdh \qquad (18)$$

Where the h_{max} is the maximum penetration depth, and the P is the indentation load referring to figure 3. Then the elastic energy (E_e) and plastic energy (E_p) can be expressed as:

$$E_e = \int_{h_f}^{h_{max}} P dh \tag{19}$$

$$\begin{aligned} E_p &= E_t - E_e \\ &= \int_0^{h_{max}} P dh - \int_{h_f}^{h_{max}} P dh \end{aligned} \tag{20}$$

Figure 27 is obtained from a loading-dwelling-unloading curve of Bi57In26Sn17 at 600mN indentation load and 10 s dwelling period. The plastic energy is represented by the pinkish-shaded area, the elastic energy is represented by the magenta color, and the total energy is the sum of the two shaded areas. In microindentation of Bi57In26Sn17 alloy, 95-96% of the total energy during indentation is dissipated through plastic deformation, whereas less than 5% of the total energy causes the elastic deformation of the sample.

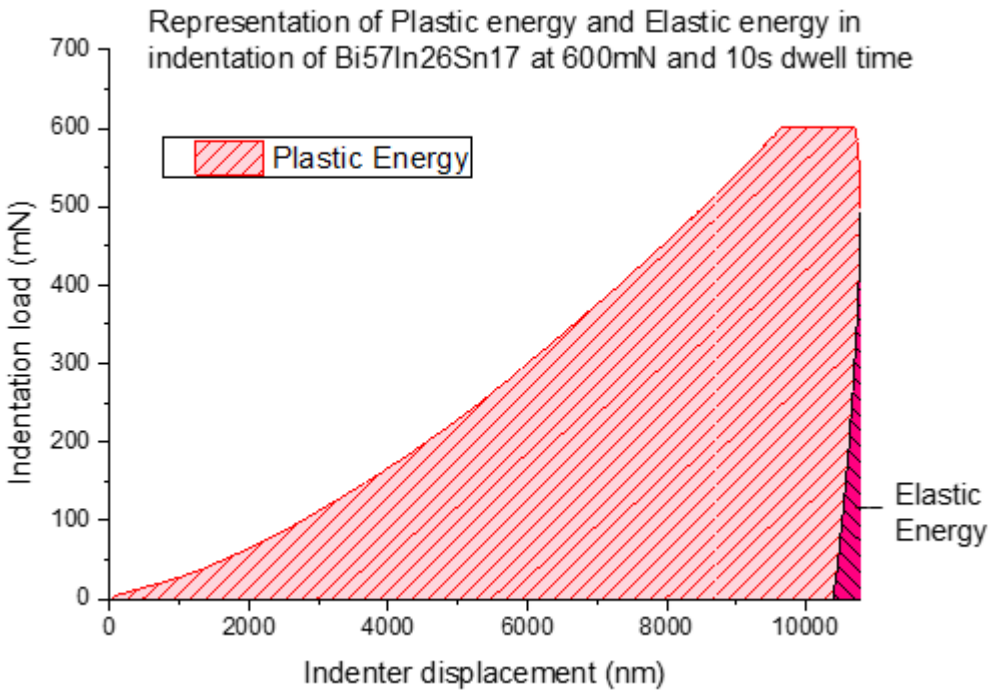

Figure 27: Representation of plastic energy and elastic energy in a typical 3-stage curve

Chapter 6 :Conclusions and future work

6.1 Summary

The main objective of this study is to use microindentation to investigate the Vickers hardness and reduced contact modulus of the Bi57In26Sn17 lead-free alloy, to achieve a better understanding of the indentation behavior of Bi-In-Sn bulk material, and provide a series of reference data for further study. This thesis, firstly, reviewed the history of micro/nano-indentation. In addition, a literature review of previous research on Bi-In-Sn alloys was completed. Reliable and efficient experiments were carried out to meet the test requirements for soft alloys like Bi-In-Sn alloy.

All the samples were processed carefully before the microindentation test, and repeatedly examined through an optical microscope as well as through a scanning electron microscope to ensure the indentation results were not affected by surface anomalies caused by human factors.

From the microindentation of Bi57In26Sn17, the following conclusions can be drawn:

1. No bulge, break point, pop-in, and pop-up observed from the load-displacement curves of the 100mN to 1000mN peak load indentation tests for a fixed dwell time, which indicates a good consistency among the indentations. Also, the imprints showed good clarity. The load

dependence of the diagonal length for different dwell times further confirmed that. The validity of the microindentation for Bi57In26Sn17 lead-free alloy data were ensured.

2. The Vickers hardness value for Bi57In26Sn17 lead-free alloy was found affected by the following factors: a). indentation depth b) dwell time.

3. The contact modulus for Bi57In26Sn17 lead-free alloy was dwell-time dependent for small dwell times, and became constant for large dwell times.

6.2 Suggestion

It was strongly recommended to prepare the Bi-In-Sn alloy sample with care, since the alloy has a low hardness value compared to most metals and ceramics. Mechanical polishing is very likely to cause material surface scratches.

The future work likely involves the use of the nanoindentation technique to study the indentation deformation of individual phases. In other words, the nanoindentation will be applied in bismuth phase, tin phase and indium phase, respectively. Apparently, this has put forward high standard on sample preparation and new methods to minimize the errors that are generated from the instrument and human operation.

Bibliography

[1] "Historical Lead Prices and Price Chart," 2006. [Online]. Available: http://www.infomine.com/investment/metal-prices/lead/all/.

[2] X.Y. Zhao, M.Q. Zhao, X.Q. Cui, T.H. Xu, M.X. Tong, Chin., *J. Nonferrous Metals., 17,* p. 805, 2007.

[3] Xu Chen, Feng Xue, Jian Zhou, Yao Yao, *J. Alloys Compd.,* p. in Press, 2015.

[4] R. M. Shalaby, *Mater. Sci.Eng. A 560,* pp. 86-95, 2013.

[5] J. Boussinesq, "Applications des Potentiels a l'etude de equilibre et du movement des solides elastiques," 1885.

[6] *ASTM E10 – 14,* 1990.

[7] I. N. Sneddon, *Int. J. Engng. Sci.,* p. 47, 1965.

[8] G. M. Pharr, W. C. Oliver, *F. R. Brotzen, J. Mater. Res.,* p. 613, 1992.

[9] H. R. Hertz, "Ueber die Beruehrung elastischer Koerper (On Contact Between Elastic Bodies)," *Gesammelte Werke (Collected Works),* 1882.

[10] S. Timoshenko and J.N. Goodier, in *Theory of Elasticity,2nd Ed.*, N.Y., McGraw-Hill, 1951.

[11] I.N.Sneddon, "“Boussinesqs problem for a rigid cone.”," *Proc. of the Cambridge Philosophical Soc.,* 1948.

[12] W. C. Oliver, R. Huntchings, "ASTM STP 889," *J. B. Pethica,* pp. 90-108, 1986.

[13] Love A.E.H., "“Boussinesq's problem for a rigid cone.”," *The Quarterly J. of Mathematics,* 1939.

[14] L.A.Galin, "“Spatial contact problems of the theory of elasticity for punches of circular shape in planar projection.”," *J. Appl. Math. Mech.(PMM),* pp. 425-448, 1946.

[15] S. I. Bulychev, V. P. Alekhin, *Zavod. Lab.,* pp. 53-76, 1987.

[16] G. M. Pharr, W. C. Oliver, F. R. Brotzen, *J. Mater. Res.,* pp. 7, 613, 1992.

[17] A. C. Fischer-Cripps, Nanoindentation, New York: Springer, 2011.

[18] W.C Oliver, G.M.Pharr, *J. Mater. Res.Vol. 19, No. 1,* 2004.

[19] M. F. Doerner, W. D. Nix, *J. Mater. Res.,* 1986.

[20] N. Dao, N. Chollacoop, K. J. van Vliet, T. A. Venkatesh, S. Suresh, *Acta Materialia,* pp. 3899-3918, 2001.

[21] K. Tunvisut, E. P. Busso, N. P. O'Dowd, H. P. Brantner, *Philosophical Magazine A,* pp. 2013-2023, 2002.

[22] Karsten Durst, Björn Backes, Mathias Göken, *Scripta Materialia,* pp. 1093-1097, 2005.

[23] N. A. Stelmashenko, M. G. Walls, L. M. Brown, Y. V. Milman, *Acta Metal. Mater.,* pp. 2855-2856, 1993.

[24] Q. Ma, D. R. Clarke, *J. Mater. Res.,* pp. 859-863, 1995.

[25] J. G. Swadner, E. P. George, G. M. Pharr, *J. Mech. Phys. Solids,* pp. 681-694, 2002.

[26] M. F. Doerner, W. D. Nix, *J. Mater. Res.,* 1986.

[27] Yueguang Wei, John W. Hutchinson, J. Mach., *Phys. Solids,* pp. 2037-2056, 2003.

[28] Gabriella Bolzon, Giulio Maier, Michele Panico, *International J. Solids and structures,* pp. 2957-2975, 2004.

[29] Min Li, Weimin Chen, Yang-Tse Cheng, Che-Min Cheng, *Vacuum,* pp. 315-320, 2010.

[30] D. Tabor, *Review of Physics in Technology,* p. 145, 1970.

[31] W.D.Nix, *Mater. Sc. Eng. A,* pp. 234-236:37-44, 1997.

[32] Y. T. Cheng, *Surface and coating technology,* pp. 417-424, 2000.

[33] W. M. Huang, J. F. Su, M. H. Hong, B. Yang, *Scripta Materialia 53,* pp. 1055-1057, 2005.

[34] C. P. J. Poole, Encyclopedic Dictionary of Condensed Matter Physics, p. 1043.

[35] ""Tin Use Survey 2007"," ITRI, 2008.

[36] M.H. Braga,_, J. Vizdal, A. Kroupa, J. Ferreira, D. Soares, L.F. Malheiros, "Computer Coupling of Phase Diagrams and Thermochemistry," p. 468–478, 2007.

[37] Fang-qiu ZU, Bing ZHOU, Xian-fen LI, Xun YI, Yi-pi, "Transactions of Nonferrous Metals," *Transactions of Nonferrous Metals Society of China,* pp. 893-897, 2007.

[38] Wislei R. Osório, Leandro C. Peixoto, Leonardo R. Garcia, Nathalie Mangelinck-Noël, Amauri Garcia, *Journal of Alloys and Compounds,* p. 97–106, 2013.

[39] R. M. Shalaby, *Materials Science&EngineeringA560,* pp. 86-95, 2013.

[40] N. C. Norman, "Antimony and Bismuth," in *Chemistry of Arsenic*, OH, ASM Internationtal, 1990, p. 2.5.2 fusible alloys pp.56.

[41] Murabayashi.US Patent 4,214,903, 1980.

[42] E.P. Wood and K.L. Nimmo, Cookson Group plc.

[43] Seung Wook Yoon, Byung-sup Rho, Hyuck Mo Lee, Choong-un Kim, and Byeong-joo Lee, *Metallurgical and materials transactions A 30A,* p. 1515, 1999.

[44] H. Kabassis, J.W. Rutter, and W.C. Winegard, *Metall. Trans.A,* pp. 1515-17, 1984.

[45] L.R. Scherpereel and E.A. Peretti, *J. Mater. Sci.vol. 2,* p. 256, 1967.

[46] R. Mahmudi, A.R. Geranmayeh, M. Bakherad, M. Allami, *Materials Science and Engineering A,* p. 173–179, 2007.

[47] S. N. Chu and J.C.M. Li, *J. Mater. Sci.,* p. 2200, 1977.

[48] P.M. Sargent, M.F. Ashby, *Mater. Sci. Technol. 8,* p. 594, 1992.

[49] Lu Shen, Pradita Septiwerdani, ZhongChen, *MaterialsScience and Engineering A 558,* pp. 253-258, 2012.

[50] Lu Shen, Pin Lu, Shijie Wang, Zhong Chen, *Journal of Alloys and Compounds 574,* pp. 98-103, 2013.

[51] M.H. Braga , J. Vizdal, A. Kroupa, J. Ferreira, D. Soares, L.F. Malheiros, *Computer Coupling of Phase Diagrams and Thermochemistry 31,* p. 468–478, 2007.

[52] A.A. El-Daly, Y. Swilem, M.H. Makled, M.G. El-Shaarawy, A.M. Abdraboh, *Journal of Alloys and Compounds 484,* pp. 134-142, 2009.

[53] Dawei Pan , Li Zhang , Jianmei Zhuang, Wenjing Lu , Rilong Zhu , Wei Qin, *Materials Letters 68,* pp. 472-474, 2012.

[54] Mulugeta Abtew, Guna Selvaduray, M. Abtew, G. Selvaduray, *Materials Science and Engineering 27,* pp. 95-141, 2000.

[55] J.F. Kuhmann, A. Preuss, B. Adolphi, K. Maly, T. Wirth, W. Oersterle, W. Pittroff, G. Weyer, M. Fanciulli, in *Proceedings of Electronic Components and Techmology Conference*, 1997.

[56] "Bolton 174," [Online]. Available: http://www.boltonmetalproducts.com/Specifications.html.

[57] "Table Top Nanoindentation Tester," [Online]. Available: http://www.csm-instruments.com/TTX.

[58] "OriginLab," [Online]. Available: http://www.originlab.com/index.aspx?go=PRODUCTS/Origin.

[59] Seung Wook Yoon, Byung-sup Rho, Hyuck Mo Lee, Choong-un Kim, and Byeong-joo Lee, *Metallurgical and materials transactions A 30A,* p. 1515, 1999.

[60] H. Kabassis, J.W. Rutter, and W.C. Winegard, *Metall. Trans., A,* pp. 1515-17, 1984.

[61] L.R. Scherpereel and E.A. Peretti, *J. Mater. Sci.,* p. 256, 1967.

VITA

Author's Name:

Ruiting Zhao

Education:

Southern Polytechnique State University, B.S. in Mechanical Engineering Technology. Degree awarded in Dec 2012.
Auburn University, Ph.D. candidate in Material Science and Engineering, started in Jan 2013. Transferred to University of Kentucky in Jan 2014.